IV. Prototype Observations

IV.1 Preliminary Considerations

Measurements of radiation-belt particle fluxes often reveal temporal variations that are unaccompanied by comparable variations of the local geomagnetic field. These temporal variations definitely indicate violation of one or more of the adiabatic invariants. For example, following large enhancements in intensity above the mean level characteristic of a specific particle energy, drift shell, and pitch angle, particle fluxes often exhibit an approximately exponential decay, apparently caused by *pitch-angle diffusion* into the loss cone. (Pitch-angle diffusion violates the first and/or second adiabatic invariant.) Large depletions of flux (resulting from nonadiabatic processes that operate during substorms) often are erased in time by a diffusive exchange of trapped particles among drift shells. This latter process, known as *radial diffusion*, can be identified with violation of the third invariant.

It must be presumed that pitch-angle scattering and cross-L diffusion do not terminate after attainment of a steady state in the radiation-belt flux distribution. Rather, these invariant-violating processes undoubtedly persist (perhaps with modified intensity) as permanent phenomena of radiation-belt dynamics. Thus, observation of the steady-state flux distribution reveals spatial structures that can be considered to arise from a dynamical balance among competing nonadiabatic source and loss processes.

The observations considered in the present chapter include examples from both of the general categories outlined above, *i.e.*, temporally varying and temporally static. Some of the particle observations reveal drift-phase organization (a consequence of processes that violate only the third adiabatic invariant). Drift-phase organization is manifested in the common occurrence of "drift-periodic echoes" in energetic proton and electron fluxes. Such events demonstrate that radial diffusion must occur. Examples of the electromagnetic and electrostatic disturbances apparently responsible for the various dynamical processes have also yielded to direct observation in recent years. These observations, when made in coincidence with measured temporal variations of the particle fluxes, indicate (for example) that particle-precipitation events are often

accompanied by bursts of electromagnetic noise. Thus, the representative observations compiled in this chapter illustrate the observational evidence upon which rests the current understanding of radiation-belt dynamics.

The observations summarized in this chapter and elsewhere in the volume have involved a variety of spacecraft. For convenience, the orbital characteristics of these spacecraft are listed in Table 9 [main source: *TRW Space Log* **10**, 84 (1972)].

Table 9. Orbital Data for Cited Spacecraft

Name of Satellite	Date of Launch	Min r/a	Max r/a	Inclination	Period, minutes	Figure Numbers
Alouette 1	28 Sept 62	1.16	1.16	80.5°	105.4	51, 52
Alouette 2	28 Nov 65	1.08	1.47	79.8°	121.4	51
ATS 1	6 Dec 66	6.59	6.59	0.2°	1436.	[b]
Elektron 3	11 July 64	1.06	2.10	60.9°	168.	55
ERS 13	17 July 64	1.03	16.39	36.7°	2352.	1
Explorer 7	13 Oct 59	1.09	1.17	50.3°	101.2	51
Explorer 12	15 Aug 61	1.05	13.12	33.3°	1585.	46, 47
Explorer 14	2 Oct 62	1.04	15.46	32.9°	2184.	1, 22, 52, 79
Explorer 15	27 Oct 62	1.05	3.72	18.0°	312.0	[c]
Explorer 26	21 Dec 64	1.05	5.11	20.2°	456.	9, 38—41, 43
Explorer 34	24 May 67	1.04	34.14	67.1°	6231.	42
Gemini 4	3 June 65	1.03	1.04	32.0°	89.0	71
Gemini 7	4 Dec 65	1.03	1.05	28.9°	89.2	71
Hitch-Hiker 1	26 June 63	1.05	1.65	82.1°	132.6	49
Injun 1	29 June 61	1.13	1.16	67.0°	103.8	32
Injun 3	12 Dec 62	1.04	1.44	70.3°	116.3	1, 51, 57, 59
Injun 4[a]	21 Nov 64	1.09	1.39	81.4°	116.3	48
Injun 5[a]	8 Aug 68	1.11	1.40	80.6°	118.3	48
OGO 1	4 Sept 64	1.04	24.45	31.1°	3840.	1
OGO 3	6 June 66	1.04	20.14	30.9°	2907.9	50, 56
OGO 4	28 July 67	1.06	1.14	86.0°	98.1	48
OV1-2	5 Oct 65	1.06	1.54	144.3°	127.5	73
OV1-14	6 Apr 68	1.09	2.56	100.0°	207.8	48
OV3-3	4 Aug 66	1.06	1.70	81.6°	136.6	48
OV3-4	10 June 66	1.10	1.74	40.8°	143.2	82
Starad	26 Oct 62	1.03	1.87	71.4°	147.8	1
Telstar 1	10 July 62	1.15	1.88	44.8°	157.8	33, 41
1962-AY1	1 Sept 62	1.05	1.11	82.8°	94.4	71
1963-38C	28 Sept 63	1.17	1.18	89.9°	107.4	1, 38, 40
1963-42A	29 Oct 63	1.04	1.06	89.9°	90.9	1, 35, 36, 71
1964-45A	14 Aug 64	1.02	1.05	95.5°	89.0	1, 51, 71

[a] Injun 4 ≡ Explorer 25; Injun 5 ≡ Explorer 40
[b] ATS-1 data: Figs. 18, 23, 41, 42, 44, 45, 50, 60, 63, 64, 66, 67
[c] Explorer-15 data: Figs. 34, 41, 53, 54, 58, 73—78, 80, 81

IV.2 Decay of Particle Flux (Inner Zone)

Electrons. Electrons injected into the inner radiation zone by a high-altitude nuclear explosion (Starfish) on 9 July 1962 have provided an unusual opportunity to measure and study the natural decay of particle fluxes as a function of time. Unfortunately, the satellite best instrumented to measure these inner-zone fluxes (Telstar 1, a communications satellite) was launched on the day following detonation, and so only meager information on the natural (pre-Starfish) inner-zone electron radiation is available. Starfish electrons have only recently decayed sufficiently to permit measurements of the natural inner belt and its temporal variations (see Section IV.6).

Observations of Starfish electrons have been made at low altitudes and low L values by instruments on the satellites Injun 1 and Injun 3. The relevant measuring instrument on each satellite was a small, heavily shielded Geiger tube which detected the electrons from their intermediate bremsstrahlung in the counter shield. Temporal observations of the post-Starfish omnidirectional electron fluxes ($E \gtrsim 2$ MeV) at $L < 1.30$ are plotted in Fig. 32 for several values of the total field intensity B (corresponding to several different altitudes above the earth) [74]. The plotted data points are not raw counting rates, but have been corrected for the Starfish-produced enhancement of the proton background (see below). These corrections proved to be significant only for $B > 0.20$ gauss.

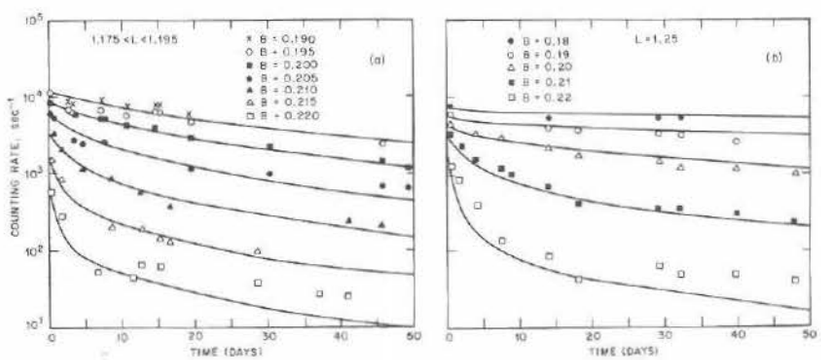

Fig. 32. Decaying inner-zone electron fluxes ($E \gtrsim 2$ MeV) observed on Injun 1 following Starfish high-altitude nuclear explosion (9 July 1962). Solid curves are predictions based on atmospheric-scattering theory for $L = 1.185$ and $L = 1.25$, respectively [74].

The solid curves in Fig. 32 were determined theoretically by assuming that the artificially injected electron population experienced decay solely in consequence of atmospheric collisions (see Section II.2). Although some uncertainties may exist in deducing the proton subtractions that ultimately yield the data points in Fig. 32, the success in fitting the observed decays with the atmospheric-scattering model suggests that other redistributive processes were comparatively insignificant during the fifty-day interval illustrated.

Instruments on the Telstar satellite made measurements of the near-equatorial inner-zone electron fluxes beginning the day after the Starfish injection (see above). The measurements were made with silicon p-n junction solid-state detectors mounted behind various entrance-collimator geometries and shield thicknesses. Data for several L values ($E > 0.5$ MeV) are shown in Fig. 33 beginning on the day following

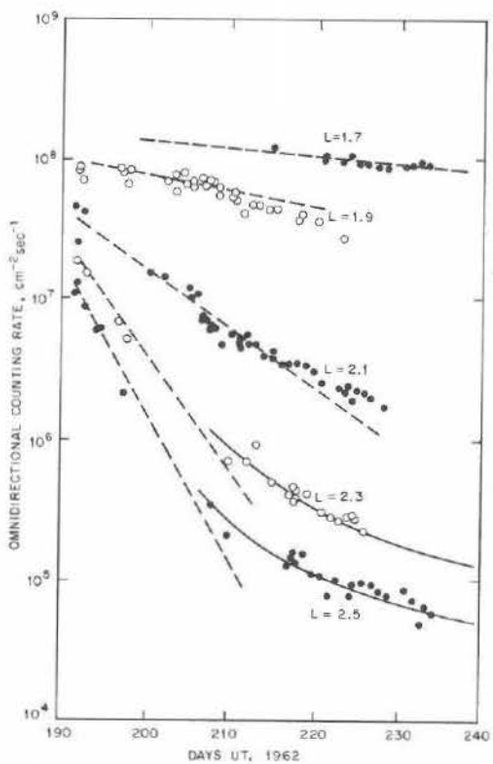

Fig. 33. Decaying inner-zone electron fluxes ($E \gtrsim 0.5$ MeV) observed near equator on Telstar 1 following Starfish event (Day 190). Solid curves and dashed lines are empirical [75].

the Starfish explosion [75]. The data were taken close to the equator at $L=1.7$ and $L=1.9$. Because of the orbital inclination, measurements at the higher L values were made at progressively higher latitudes (*e.g.*, latitude 30° at $L=2.5$).

After the explosion (Day 190) the electron fluxes exhibited approximately exponential decay until about Day 230. The apparent deviation from exponential decay at the higher L values ($L \geq 2.3$) and the later times (from approximately Day 210) actually arises from the response of the detector to inner-zone proton contamination. The lifetimes extracted from the initial exponential decays are much shorter at the higher L values than those predicted by an atmospheric-scattering model [42]. Indeed, the decay times actually *decrease* with increasing L, in explicit contrast to the prediction of any reasonable atmospheric-scattering model, *i.e.*, lifetimes *increasing* with altitude. These observations were among the first to suggest that wave-particle interactions are important in controlling magnetospheric particle dynamics.

The pitch-angle distribution of electrons injected by a high-altitude nuclear explosion is typically abnormal in the sense that few of the particles mirror near the equator (unless, of course, the detonation is equatorial). A very interesting observational result based on the USSR detonation of 28 October 1962 (Day 301) is the restoration of a pitch-angle distribution to the fundamental mode of pitch-angle diffusion. The electron measurements confirming this phenomenon were made with a shielded solid-state *p-n* junction detector flown on the near-equatorial satellite Explorer 15. Decay of the initially anomalous pitch-angle distribution to its lowest normal mode is illustrated sequentially in Fig. 34 [43]. Here the electron omnidirectional counting rates beginning with Day 301 are plotted as a function of $X \equiv [1-(B_e/B)]^{1/2}$, where B_e is the equatorial magnetic-field intensity. Most electrons injected by the nuclear blast appeared initially with equatorial pitch-angle cosine $\gtrsim 0.6$; the omnidirectional electron flux at $L=1.9$ initially exhibited an off-equatorial maximum (at $X \approx 0.8$). The initial distribution of equatorial pitch angles can be viewed as a superposition of normal modes. Each normal mode decays at a characteristic rate, with the longest lifetime belonging to the lowest eigenmode. This lowest mode is the normal pitch-angle distribution toward which the initial distribution decays. The off-equatorial peak in omnidirectional flux disappears rather quickly (in about ten days), and the lowest normal mode is essentially isolated after about thirty days. The entire pitch-angle distribution, operating in its lowest normal mode, then decays with a particle lifetime ~ 40 days.

The decay of a naturally occurring, nearly monoenergetic, electron enhancement near the inner edge of the inner belt was observed during

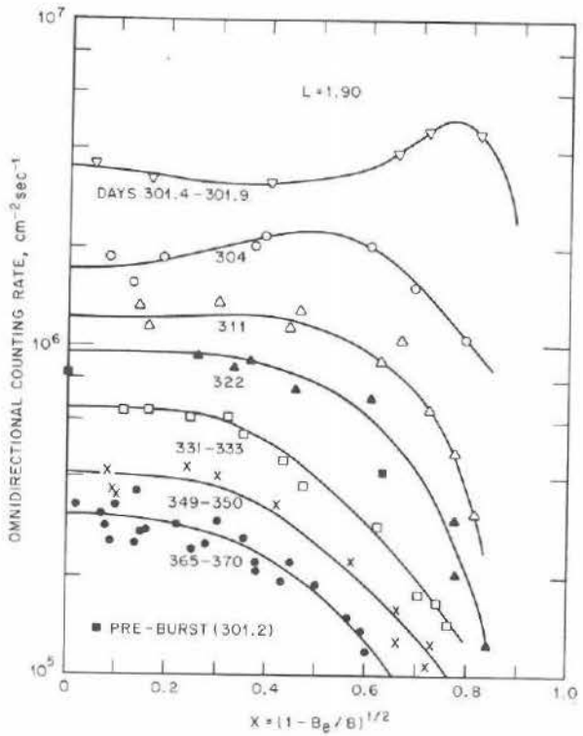

Fig. 34. Decaying omnidirectional intensities of inner-zone electrons ($E > 1.9$ MeV) observed on Explorer 15 following nuclear event of 28 October (Day 301) 1962. Solid curves are empirical [43].

a one-week period in 1963 following a magnetic storm on October 30 [76]. The relevant data were obtained with a plastic scintillation spectrometer flown on the earth-oriented, polar-orbiting satellite 1963-42A. The observed spectral peak was centered at approximately 1.3 MeV and exhibited a full width ≈ 0.23 MeV at half maximum (approximating the limit of instrumental resolution). The approximately exponential decay (with time) of the peak intensity at each of several L values is illustrated in Fig. 35 and compared there with the decay predicted by atmospheric-scattering theory. As was observed in the decay of the Starfish electrons (Fig. 32), the decay rates at these low L-values are consistent with the interpretation that electrons are lost solely through collisions with atmospheric constituents.

The apparent displacement (≈ 440 km) of the dipole axis from the earth's center permits the observation of particles locally trapped by

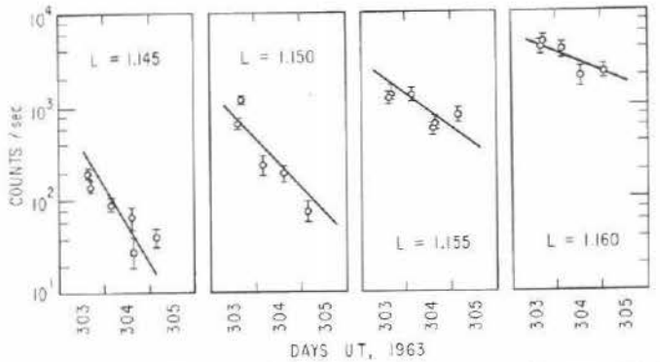

Fig. 35. Decaying omnidirectional intensities of inner-zone electrons ($E > 1.3$ MeV) observed on 1963-42A following a natural "injection" event on 30 October (Day 303) 1963. The range in B is 0.2119—0.2222 gauss. Solid curves are predictions based on atmospheric-scattering theory [76].

the magnetic field but doomed ultimately to precipitate. The 440-km displacement contributes to an "anomalously" weak-field condition (≈ 0.25 gauss, *vs* 0.31 gauss in the centered-dipole model) at sea level in the South Atlantic region. Many inner-zone drift shells thus plunge deep into the atmosphere in the vicinity of the "anomaly", while tracing a constant mirror-field intensity. Particles locally trapped on such drift shells are destined to precipitate as they drift into the "anomaly" region. Most of the actual inner-zone electron precipitation occurs here, although the pitch-angle diffusion responsible for this precipitation is distributed among all magnetic longitudes.

Indirect studies of the L-dependent decay rates of inner-zone electrons have been made by studying azimuthal variations in the low-altitude fluxes of precipitating electrons. The intensities of electrons that will mirror below the 100-km altitude exhibit significant variations with longitude. These azimuthal variations are attributed to the pitch-angle diffusion produced by atmospheric scattering and wave-particle interactions as the electrons drift from west to east. The fluxes are found to be higher to the west of the "anomaly" than to the east of it.

The general increases in electron intensity with increasing east longitude beyond the "anomaly" suggest an L-dependent pitch-angle diffusion process operating in the presence of a contracted loss cone. On each L shell, restoration of pitch-angle isotropy via diffusion is prevented only by precipitation into the atmosphere, which typically occurs at the "anomaly" (where the loss cone abruptly expands). Measurements of the electron flux at various drift phases of an adiabatic drift shell can thus be used to extract a pitch-angle diffusion coefficient. Examples

of the azimuthal variation of the fluxes of electrons ($E > 0.4$ MeV) that would mirror in the "anomaly" at altitudes < 100 km are shown in Fig. 36 [77]. These data, obtained with a plastic scintillation detector attached to a photomultiplier flown on the polar orbiting vehicle 1963-42A, are plotted as a function of longitude measured (in degrees) eastward from the South Atlantic "anomaly".

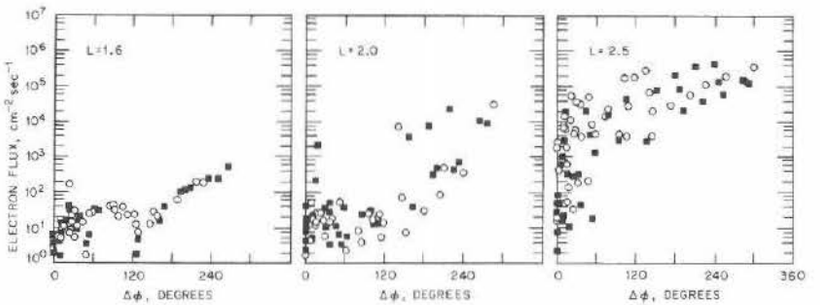

Fig. 36. Daytime (open circles) and nighttime (filled squares) measurements of omnidirectional flux of electrons ($E > 0.4$ MeV) that would mirror in the "anomaly" ($\Delta\varphi = 0$) at altitudes < 100 km [77], obtained at various magnetic longitudes (φ) on three separate B, L contours.

Protons. High-energy protons trapped in the earth's magnetic field and mirroring at low altitudes were first detected (and their energy spectra measured) by the use of recoverable nuclear-emulsion packets flown on rockets and satellites. A large number of these emulsion packets were flown during the years 1961—64, yielding much data on the temporal decay of the Starfish-produced proton fluxes.

Recovered emulsion records indicating the flux of protons ($E \sim 55$ MeV) in the South Atlantic "anomaly" were divided into altitude increments and then examined as a function of time. The proton intensities for altitudes of 440 km and 350 km are shown in Fig. 37 [78]. The dashed vertical lines indicate the day of the Starfish explosion. Subsequent to July 1962, the Starfish-enhanced proton fluxes decayed steadily with time toward their pre-Starfish levels. The solid curves drawn through the data points represent the theoretically expected fluxes (above the natural level) of Starfish protons, assuming that ionization of the atmosphere (see Section II.2) is the only loss mechanism for these protons. The drift-averaged values [41] of atomic-electron densities $\Sigma Z_i \bar{N}_i$ [*cf.* (2.04)], using the Harris-Priester model atmosphere

[79] below 1000 km, are noted for each observation altitude in Fig. 37. The agreement between the observations and the theoretical predictions is very good. This result suggests that the ionization theory, incorporating the model atmosphere, is sufficient to account for the decay of Starfish-produced proton fluxes observed at these low altitudes.

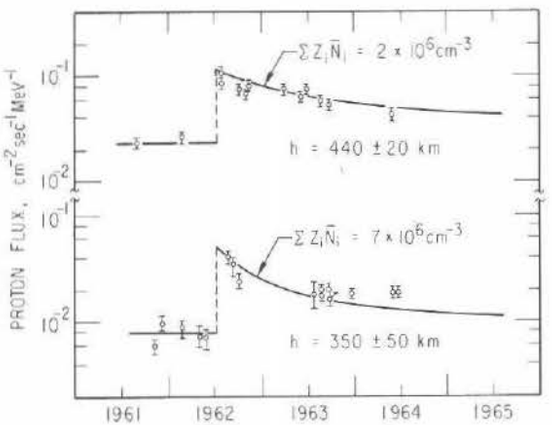

Fig. 37. Inner-zone omnidirectional proton flux ($E = 55$ MeV) measured at sporadic times in two altitude ranges above the South Atlantic "anomaly". Sharp increases (dashed lines) coincide with Starfish event (9 July 1962). Solid curves post-Starfish are predictions based on atmospheric-collision theory [78], assuming a source sufficient to maintain the mean pre-Starfish intensity (horizontal solid lines). Post-Starfish curves are normalized to the first data point measured at each altitude following the nuclear event.

IV.3 Decay of Particle Flux (Outer Zone)

Electrons. Extensive studies of the outer radiation belt have shown that decay begins to predominate two or three days after a magnetic storm produces enhancements of the electron flux. The electron intensities then decay in an approximately exponential manner, as in the inner zone.

The typical temporal behavior of outer-zone electron fluxes (rapid increases during storms, followed by steady decays) can be seen readily in Fig. 38 where a four-month time history of electron fluxes ($E > 1$ MeV) is plotted at each of three different L values [80]. Both high-altitude (Explorer-26) and low-altitude (1963-38C) satellite data are plotted at each L value in order to compare the fluxes measured at different

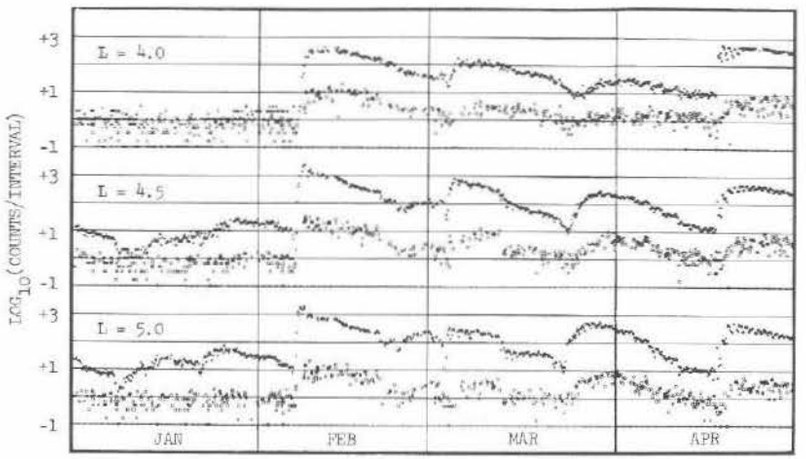

Fig. 38. Unidirectional counting rates of electrons observed on polar-orbiting satellite 1963-38C ($E > 1.2$ MeV, open squares) and on near-equatorial satellite Explorer 26 ($E > 1.0$ MeV, crosses) during four months in 1965 [80]. One count per interval represents a flux ≈ 1200 cm^{-2} sec^{-1} ster^{-1}.

locations in a given flux tube. The data were obtained with solid-state detectors.

The steady decay of flux observed after storm-produced enhancements is occasionally interrupted by short-term variations (either increases or decreases) that last for several hours to a day. These variations, superimposed on the long-term decay, have been identified as adiabatic modulations caused by gradual time variations of the local magnetic field intensity on a given L shell. These gradual changes in the local field intensity result primarily from temporal changes in the low-energy (~ 25-keV) proton density in the quiet-time ring current, whose density generally peaks at $L \sim 6$. Additional adiabatic modulation may arise from changes in the intensity of currents flowing on the magnetosphere boundary.

As in the case of inner-zone electron fluxes, the e-folding times extracted from the approximately exponential decays of outer-zone fluxes following the storm-time enhancements can be taken as estimates of electron lifetimes. The lifetimes measured for selected L values and energies following the storm of 18 April 1965 are shown in Fig. 39 [80]. Electron lifetimes are thus found to vary directly with energy and inversely with L in the outer radiation zone.

Natural enhancements of the electron flux, especially in the region $L \approx 3.0$—3.5, were observed in association with the large storm of 18

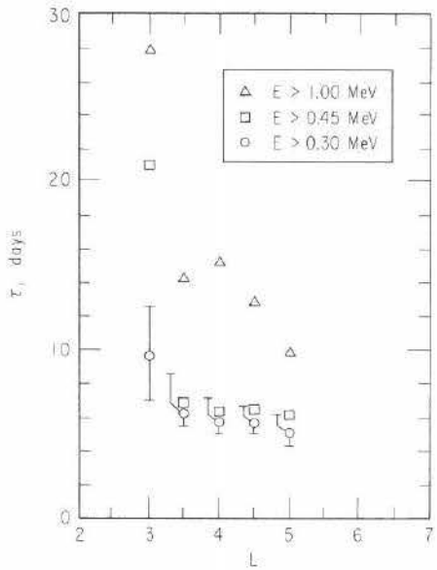

Fig. 39. Lifetimes of near-equatorial unidirectional electron fluxes, as determined from Explorer-26 data (see Fig. 38) for the period 22.5 April 1965 to 3.0 May 1965 [80].

April 1965. At both high and low altitudes in this region, the enhanced fluxes were observed to decay more quickly during the first few days following "injection" than during the subsequent quiet period (see Fig. 40). No similar temporal change in the decay rate is apparent outside this narrow interval of L [80]. In view of the nonlinear processes (Section II.6) that tend to act upon enhanced particle fluxes, it is perhaps quite reasonable to expect such behavior in the region where storm-associated particle injection is most intense.

The e-folding decay times of Fig. 39, determined from the flux decays following the storm of 18 April 1965, are comparable to the generally accepted lifetimes that enter most discussions of pitch-angle diffusion. This can be seen from the electron lifetimes plotted in Fig. 41. These decay times were measured from data obtained at various epochs by instruments on four different elliptically orbiting satellites [43] and on the synchronous satellite ATS 1 ($r=6.6a$). The data were obtained over approximately a five-year period. The overall similarity of the lifetimes from one determination to another suggests that the basic magnetospheric processes acting to produce the pitch-angle diffusion persist from year to year.

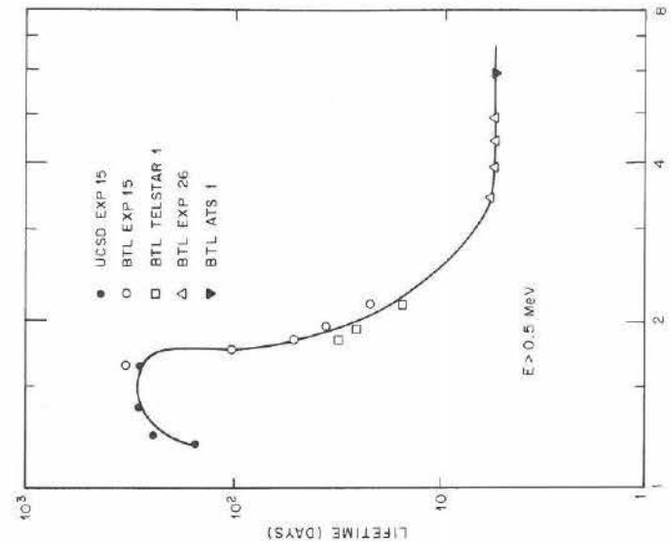

Fig. 41. Observed lifetimes of near-equatorial electron fluxes in the inner and outer zones [43].

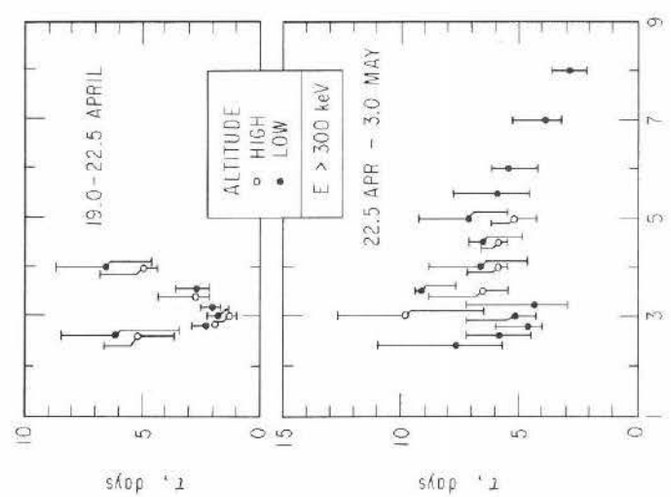

Fig. 40. Lifetimes of near-equatorial (Explorer 26) and low-altitude (1963-38C) unidirectional electron fluxes [80]. These lifetimes are determined for two successive time intervals following the magnetic storm of 18 April 1965 (see Fig. 38).

Protons. Pitch angle diffusion is not ordinarily known to affect radiation-belt protons at energies $E \gtrsim 1$ MeV. There exists no observational evidence to suggest that such protons fail to obey (3.57) deep in the inner magnetosphere ($L \lesssim 1.7$). In the outer magnetosphere, however, the fluxes of energetic protons ($E \sim 5$—70 MeV) are observed to rise and decay on time scales ~15 minutes. Such observations (see below) must be interpreted with caution in the context of particle diffusion, since solar-flare protons often apparently have free access to the synchronous orbit ($r = 6.6a$) where the observations [81] have been made.

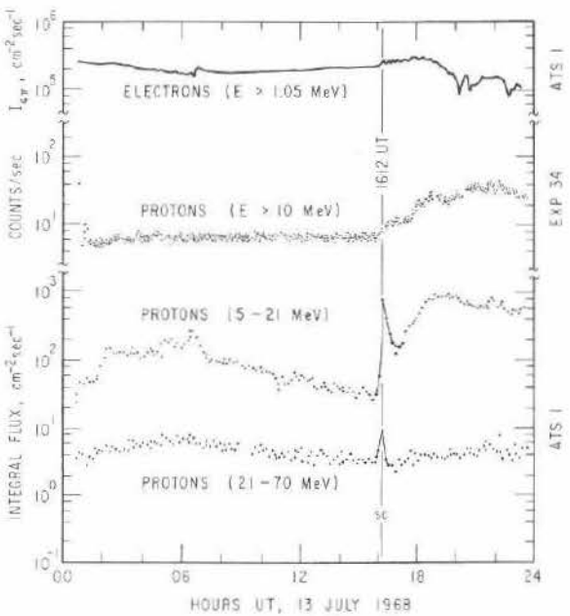

Fig. 42. Omnidirectional fluxes of solar protons and outer-belt electrons observed at synchronous altitude on ATS 1, and of solar protons ($E > 10$ MeV) observed simultaneously in interplanetary space on Explorer 34 [81].

In Fig. 42, a proton enhancement at synchronous altitude accompanies the sudden commencement (1612 UT, 13 July 1968) of a magnetic storm, and subsequently decays on a time scale ~15 min in the absence of further magnetic-field variation at synchronous altitude [81]. In a similar event on 20 November 1968 (see Fig. 67, Section IV.8), the decay was modulated by drift-periodic echoes (see Section III.1) in the proton flux, indicating the presence of closed drift orbits. In this observation, the proton population observed at the satellite near local

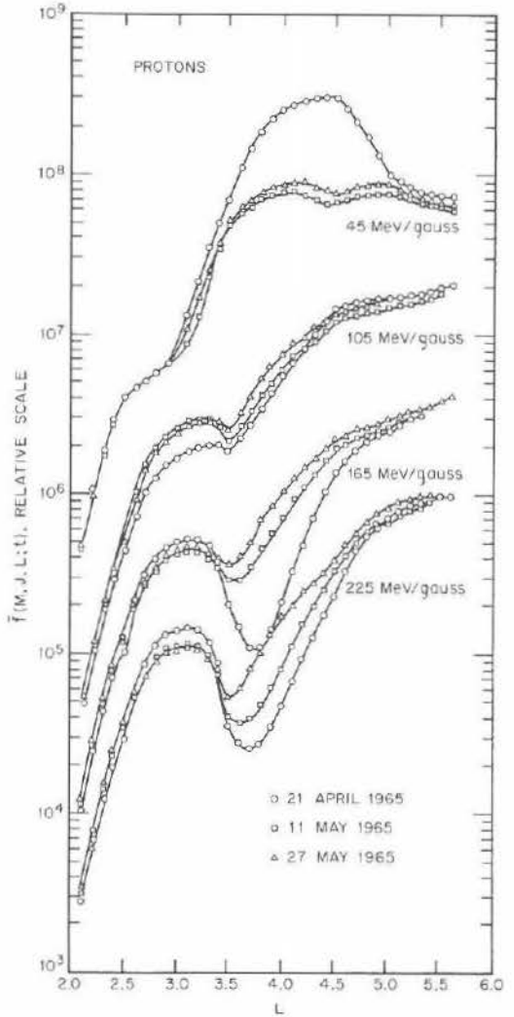

Fig. 43. Temporal evolution of proton distribution function at $J = 0$ following magnetic storm of 18 April 1965 [82], based on Explorer-26 data.

midnight apparently does not have free egress to interplanetary space. The value of ε (see Section I.1) is rather large (~0.1) for the behavior of these protons to be interpreted in terms of adiabatic theory, however. Thus, there may be a fractional probability on each drift period for a proton to escape the magnetosphere.

The proton decay rate in Fig. 42 clearly increases with proton energy, as an interpretation based on the breakdown of adiabatic theory ($\varepsilon \gtrsim 0.1$) would lead one to expect. On the other hand, ground-based observations of storm-associated geomagnetic micropulsations suggest the presence of adequate spectral intensity near $\omega/2\pi \sim 1$ Hz to account for the rapid decay rates observed. In the magnetosphere, these Pc-1 micropulsations (ion-cyclotron mode) could interact with the protons through a Doppler-shifted cyclotron resonance (see Section II.5), thereby causing pitch-angle diffusion.

At proton energies $E \lesssim 0.5$ MeV, the evidence for pitch-angle diffusion is unequivocal. In Fig. 43, the interstorm (18 April to 15 June 1965) evolution of $\bar{f}(m,J,L;t)$ at $J=0$ is illustrated for selected values of M [82]. The pronounced decay between 21 April and 11 May at $M=45$ MeV/gauss illustrates the operation of a nonlinear mechanism (*cf.* Section II.6) for self-limiting of the trapped proton flux. Once the stable limit is achieved, the decay ceases (*cf.* 11—27 May). The contrasting behavior of $\bar{f}$ at $M=225$ MeV/gauss and $L \gtrsim 3.5$ is evidence for radial diffusion (inward from a source beyond $L \approx 5$ and outward from an apparent source at $L \approx 3$). The distribution function clearly increases with time in the region $3.5 \lesssim L \lesssim 4.5$ so as to fill the "slot" between regions of higher radiation intensity (*cf.* Section IV.6).

IV.4 Statistical Observations

Extended observations of the electron-radiation environment at synchronous altitude have been carried out from the satellite ATS 1. A compilation of ATS-1 data on the integral omnidirectional flux $I_{4\pi}$ above four energy thresholds is illustrated in Fig. 44 [83]. The results are presented in the form of a probability P that the flux $I_{4\pi}$ will exceed a given level Q. For $0.1 \lesssim P \lesssim 0.6$, this probability is quite linear with respect to $\log Q$. Extrapolation of the linear fits to $P=1$ and $P=0$ permits definition of a "maximum" flux I^* and a "minimum" flux $I_{\min}$ for each energy threshold.

Two properties of Fig. 44 are immediately apparent. First, the value of $\log I^*$ increases with decreasing energy threshold. Second, the range of probable fluxes, as measured by $\Delta \log I \equiv \log(I^*/I_{\min})$, narrows with decreasing energy. These properties are shown quantitatively in Fig. 45. Extrapolation of the results to $E=40$ keV [*cf.* (2.69a) for $s=0.5$, $B=125\gamma$, $N_e=1\,\mathrm{cm}^{-3}$] yields $I^*(E^*) \sim 10^8\ \mathrm{cm}^{-2}\,\mathrm{sec}^{-1}$, in good agreement with (2.72). Moreover, the value of $\Delta \log I$ is approximately 0.18 at $E=E^*=40$ keV, *i.e.*, the probable fluxes (as identified by linear extrapolation in Fig. 44) lie within the range $0.6I^*$ to $1.0I^*$ at $E=E^*$.

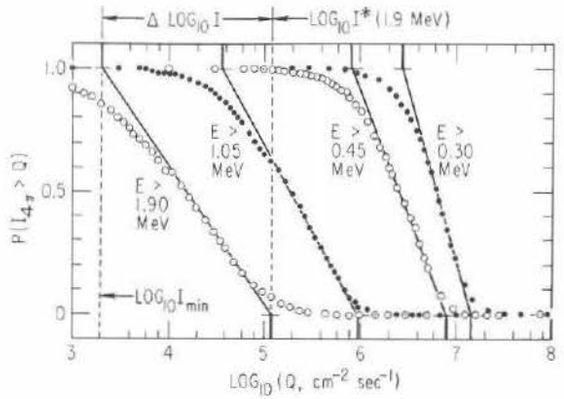

Fig. 44. Compilation of ATS-1 electron data [83], showing the probability P that the integral omnidirectional flux $I_{4\pi}$ exceeds a specified value Q. Solid lines empirically fit the data points for $0.1 \lesssim P \lesssim 0.6$.

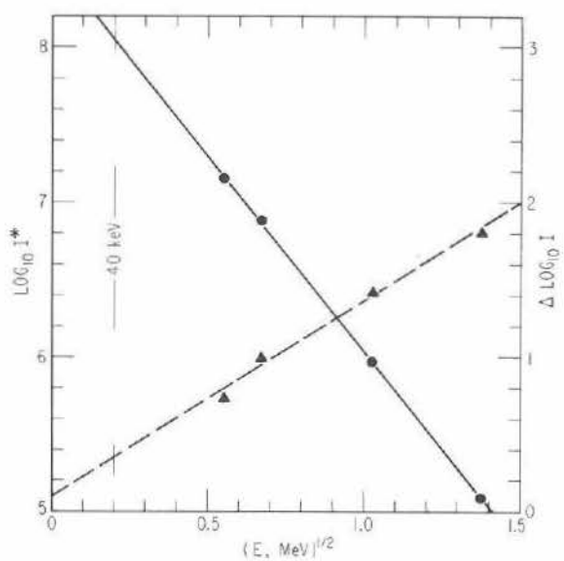

Fig. 45. Dependence of $\log I^*$ (circles) and $\log(I^*/I_{\min}) \equiv \Delta \log I$ (triangles) on threshold energy E. Solid lines empirically fit the intercepts extracted from Fig. 44. The unusual choice of abscissa facilitates extrapolation to the lower energies.

The self-limiting property of synchronous-altitude electron fluxes thus enforces a very narrow range of flux variability at $E \approx E^*$. The magnetosphere apparently becomes increasingly tolerant of integral-flux variability for particle energies well above E^*, the threshold for cyclotron resonance with a growing wave.

IV.5 Static Flux Profiles

In the absence of temporal variations in the observed particle fluxes, it is frequently possible to obtain information about competing dynamical processes from observations of the steady-state distributions. In view of the multiplicity of unobserved processes that may be competing, such steady-state distributions must always be interpreted with special caution. However, there are a number of steady-state observations that suggest a prominent role for radial diffusion at constant M and J.

Protons. Extensive measurements of the lower-energy proton distributions (100—500 keV) in the magnetosphere have been made by scintillation-counter detectors flown on the satellites Explorer 12, 14, 15, and 26. These particle populations are found to be very stable in time and to have energy spectra that are exponential over a wide range of energy and L. Further, the spectra harden with decreasing L. Three spectra obtained at different L values in 1961 on Explorer 12 are shown

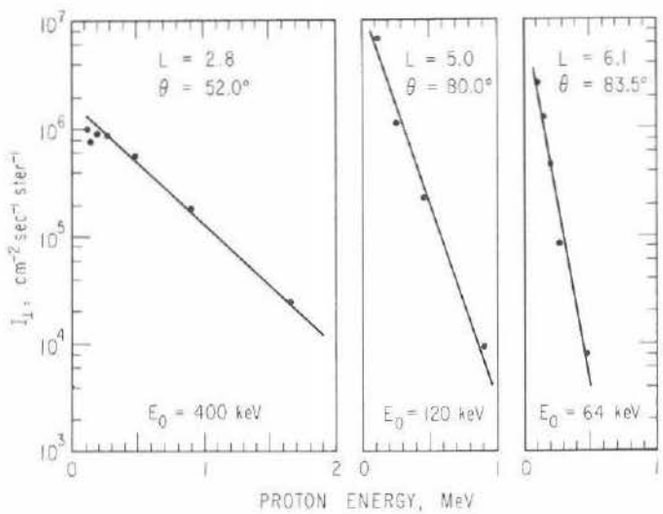

Fig. 46. Outer-zone proton spectra observed [84] on Explorer 12 (26 August 1961).

in Fig. 46 [84]. More recent magnetospheric proton spectra for energies between 0.17 MeV and 3.4 MeV have been obtained from an instrument on satellite 1964-45A in 1964 and 1965 [85]. Where comparisons are possible, these data agree with those obtained earlier (in 1961).

It is found empirically from data such as those in Fig. 46 that E_0, the e-folding energy of the exponential proton spectrum, varies as L^{-3}; *i.e.*, in direct proportion to the equatorial field intensity B_e. This variation of E_0 with B_e is often cited as evidence for radial diffusion at constant M and J. Such a claim probably overstates the case. What can be shown is that any steady-state ($\partial \bar{f}/\partial t = 0$) solution of (3.01) (the equation governing radial diffusion at constant M and J, excluding other dynamical processes) has the property that $(\partial \ln \bar{f}/\partial \ln p)_{L,y}$ is independent of L for particles having the same J^2/M if D_{LL} and all boundary locations are independent of particle energy[33].

For nonrelativistic particles ($E = p^2/2m_0$) it is convenient to represent a power-law energy spectrum as $J_\perp(E) = J_\perp(p_0^2/2m_0)(p_0/p)^{2l}$ and an exponential spectrum as $J_\perp(E) = J_\perp(0)\exp(-p^2/2m_0E_0)$. The statement concerning the L-independence of $(\partial \ln \bar{f}/\partial \ln p)_{L,y}$ in the steady state implies that

$$(\partial \ln \bar{J}_\perp/\partial \ln p)_{L,y} = 2 + (\partial \ln \bar{f}/\partial \ln p)_{L,y} = \text{constant} \qquad (4.01)$$

on a surface of constant M and J in phase space. The power-law spectrum retains its form with p_0 and l independent of L. The exponential spectrum retains its exponential form, but E_0 varies with L in such a manner that $E_0(L) \propto 1/y^2L^3$. In other words, the e-folding energy of the exponential spectrum behaves like the energy of an individual particle.

In view of the energy dependence of competing dynamical processes (including radial diffusion caused by electrostatic impulses; *cf.* Section III.3) it is quite remarkable that the observations of E_0 satisfy (4.01), even at $y = 1$. Even more remarkable is that the observations appear to satisfy (4.01) at all other values of y. In Fig. 47 the observed e-folding energy E_0 is plotted against L for selected values of $\sin^{-1} y_7$ [86]. The "theoretical" curves appear to converge on a common value of E_0 at $L \approx 10$. This latter location can perhaps be interpreted as the location of the proton source.

These data at most *suggest* the inward radial diffusion of the protons to lower L values from an external source. In view of possibly competing energy-dependent processes, the data could perhaps be interpreted in other ways. Furthermore, the application of (4.01) yields no specific

[33] Under these stringent conditions, the solutions $\bar{f}$ corresponding to two distinct values of E_7 (see Fig. 24, Section III.1) can differ only by a multiplicative factor independent of L, in view of the "uniqueness" of steady-state solutions to (3.01).

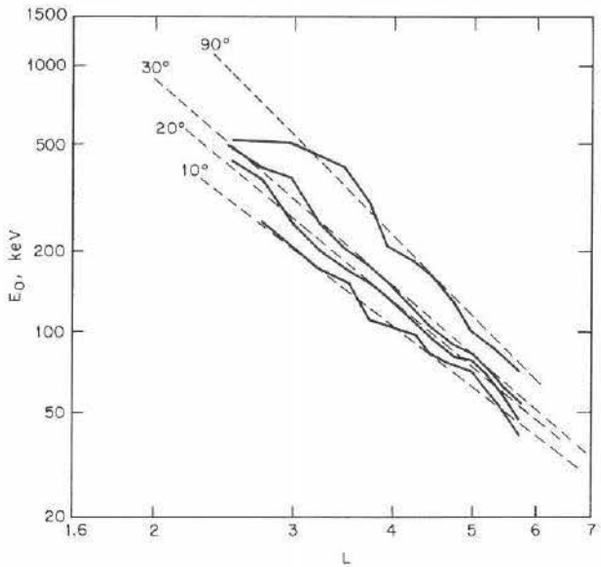

Fig. 47. Empirical e-folding energies (solid curves) of observed proton spectra [84] at y values consistent with (3.02); expected variation (dashed curves) of energy with L for individual protons having constant M and J, at selected values of E_γ and $\sin^{-1} y_\gamma$ [86].

magnitude for the diffusion coefficient allegedly responsible for establishing the observed distributions. The radial transport coefficient must be obtained from considerations other than the time-independent particle data.

Heavier Ions. The presence of alpha particles (and heavier ions), as well as protons, in the radiation belts offers a possible opportunity to select a dominant radial-diffusion mechanism from Chapter III. Conventionally, fluxes of alpha particles and protons are compared at the same energy per nucleon (see Section III.3) so as to obtain the alpha-to-proton (α/p) ratio as a function of L. Values of this ratio are indicated[34] for $L\sim 3$ in Fig. 48 [59]. An energy of ~ 0.5 MeV at $L\sim 3$ scales (at constant M and J, with $J=0$) to ~ 10 keV at $L\sim 10$, where interplanetary ions may be expected to enter the magnetosphere.

At the same energy/nucleon, the solar-wind [9] and solar cosmic-ray [88] α/p ratios (~ 1—20×10^{-2}) are substantially larger than the values

[34]The decay of the α/p ratio (Fig. 48) between 8 November 1968 and 26 January 1969 follows an enhancement accompanying the magnetic storm of 1 November 1968.

~ 1—20×10^{-4} plotted in Fig. 48[35]. If the magnetospheric helium-ion source is solar[36], then helium nuclei are either lost more quickly than protons at a given L value or they diffuse inward more slowly. A consideration of possible loss mechanisms (*cf.* Sections II.2 and II.5) tends to rule out the former possibility. Since a helium ion with the same energy/nucleon as a proton has a larger azimuthal-drift speed than the proton, helium ions would tend to diffuse inward (under electrostatic fluctuations with an ω^{-2} spectral density) more slowly than pro-

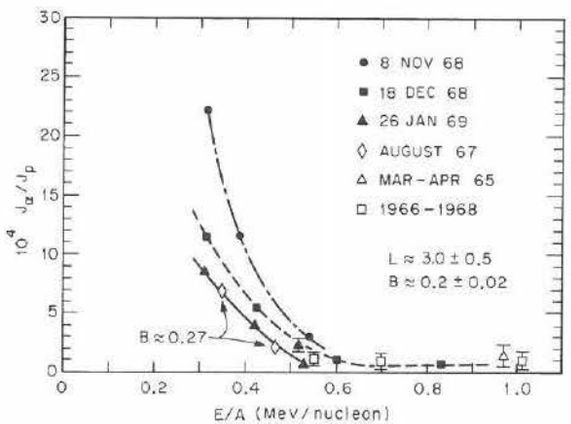

Fig. 48. Low-altitude observations of α/p ratio (based on comparison of $J_\perp$ values) at several different epochs [87].

tons. There would be no difference among radial diffusion coefficients caused by an inverse-square *magnetic* power spectrum. Radial diffusion of solar helium ions by electrostatic (rather than electromagnetic) impulses (see Section III.3) thus apparently can account for the reduced helium-to-proton ratio observed in the inner magnetosphere [40]. This latter conclusion depends upon assumptions concerning the ion source and cannot be extrapolated without thought to all energies. However, any indication of radial diffusion driven by electrostatic impulses tends to cast doubt on the customary interpretation of Figs. 46 and 47.

[35]The values shown in Fig. 48 were obtained from low-altitude (high-latitude) observations. Recent equatorial measurements [87] suggest an α/p ratio ~ 1—20×10^{-2} at $E/A\sim 0.4$ MeV/nucleon, for $3.1\lesssim L\lesssim 4.4$.

[36]Alternatively, the source for magnetospheric helium radiation might be ionospheric, in the form of He^+ ions blown into the earth's plasma sheet by the polar wind [89].

Electrons. It is much more difficult to study the spectral and spatial parameters of outer-zone electron fluxes than of proton fluxes, since the former vary so drastically with time (*cf.* Fig. 38). However, several studies of this nature are on record. In one such study the spectral parameter E_0 for electrons ($E=1$—$4\,\mathrm{MeV}$) was obtained from data measured by a scintillation spectrometer on the low-altitude satellite Hitch-Hiker 1 during July and August 1963. The results are plotted in Fig. 49 as a function of L for several days in July [90]. The solid line indicates an empirical hardening of the spectrum with decreasing L, given by $L^{1.3}E_0=2.4\,\mathrm{MeV}$.

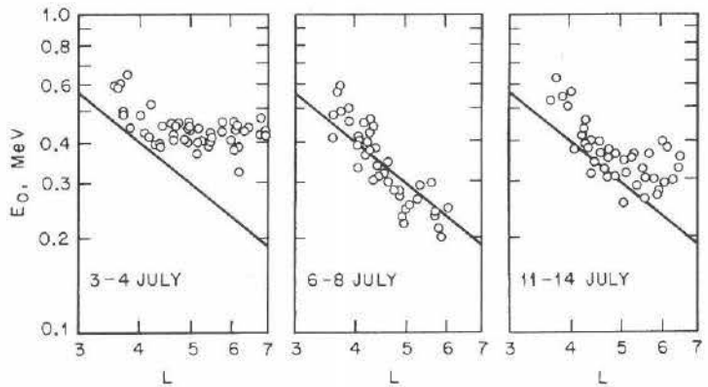

Fig. 49. Empirical e-folding energies (open circles) of electron spectra ($E=1$—$4\,\mathrm{MeV}$) observed during three periods in July 1963 [90]. Coverage on 4 July extends from 00 UT to 03 UT; the other eight days have 24-hour coverage. Solid lines correspond to $L^{1.3}E_0=2.4\,\mathrm{MeV}$.

During the period of 3—4 July, the spectral parameter evidently became L-independent beyond $L\sim4$. During the geomagnetically more active period of 6—8 July, the spatial variations in the spectral parameter E_0 agreed qualitatively with that "expected" from (4.01). The distinction between quiet and disturbed times could possibly be taken to mean that radial diffusion at constant energy (via drift-shell splitting; see Section III.7) dominates that at constant M and J during quiet intervals.

The phenomenon of drift-shell splitting has been verified by a comparison of data obtained with electron spectrometers on the ATS-1 and OGO-3 satellites [91]. The diurnal variation of electron fluxes (higher at noon than at midnight) and pitch-angle distribution ($J_{\pi/2}>J_{\pi/3}$ at noon; $J_{\pi/3}>J_{\pi/2}$ at midnight) observed at fixed energy on ATS 1 are found to be adiabatically compatible (at least during quiet periods)

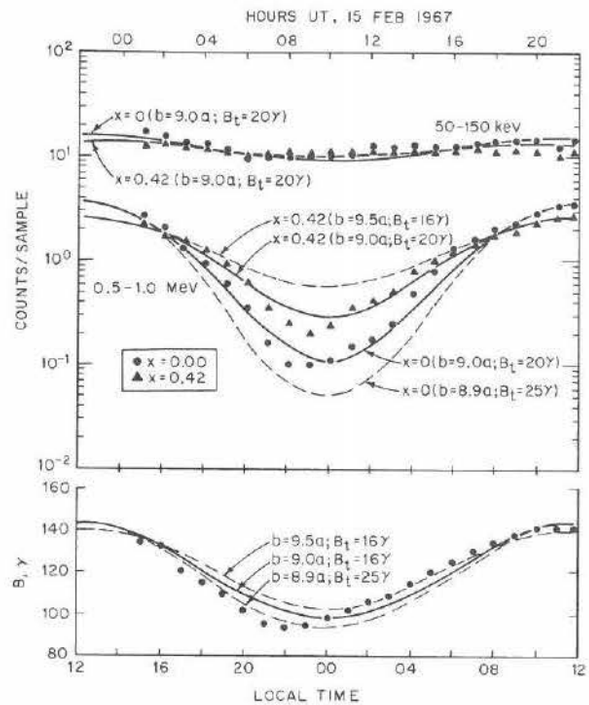

Fig. 50. Diurnal variation of electron fluxes and magnetic field (data points) observed at synchronous orbit (ATS 1), as compared with predictions (dashed and solid curves) based on Mead-Williams field models ($b/a, B_t$) and distribution function $\bar{f}(M,J,\Phi)$ deduced from OGO-3 electron data [91].

with the flux profiles obtained over a broad range of L values from the OGO-3 data (see Fig. 50). Although drift-shell splitting is thus established as an adiabatic phenomenon (see Section I.7), its quantitative influence on radial diffusion can be determined only by inserting a pitch-angle diffusion coefficient (either measured directly, or deduced from an exponential decay rate) in (3.37). When this is done (see Section IV.6), it is found that shell splitting effects can seldom account for even 10% of the observed radial diffusion. The correct interpretation of Fig. 49 is probably other than one based on constant-energy diffusion.

Finally, Fig. 51 illustrates the yearly "history" of the outer electron belt during a period of decreasing solar and geomagnetic activity (decreasing K_p) in terms of the "crest" position L_c of three integral unidirectional-flux profiles [92]. These annual-mean crest positions could be regarded as quasi-static features of the radiation belt, resulting from the balance between loss (pitch-angle diffusion) and transport (radial diffusion) pro-

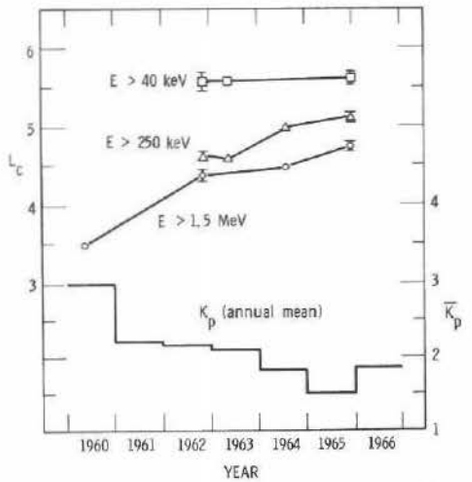

Fig. 51. Variation of outer-zone electron-flux crest positions ($L_c \equiv$ shell corresponding to maximum electron $I_\perp$) during a period of decreasing geomagnetic activity [92], as indicated by $\bar{K}_p$ ($\equiv$annual mean of K_p).

cesses operative during the year. The essential difficulty in interpreting Fig. 51 is that the flux profiles are considered for fixed energy, whereas the radial-diffusion process is believed to operate at constant M and J. It is preferable, therefore, to examine profiles of $\bar{f}(M,J,L)$ at fixed M and J (*cf.* Fig. 43, Section IV.3).

IV.6 Time-Varying Flux Profiles

The most convincing evidence for the radial diffusion of radiation-belt particle fluxes has arisen from studies of temporal variations in the flux profiles (distributions in L). Most frequently, these studies examine the changes in the trapped-electron fluxes following storm-time enhancements. Most of the reported inward movements of flux profiles observed in the trapped-electron intensities have been especially evident in the higher-energy ($E \gtrsim 1$ MeV) fluxes. This last observation may be understood qualitatively by recalling the observed energy dependence of electron lifetimes plotted in Fig. 39. Although radial diffusion could well be important for electrons of energy $E \sim 0.5$ MeV, their observed temporal development may be dominated by the persistent decay due to pitch-angle diffusion. The higher-energy electrons, with longer lifetimes, then survive to exhibit the strongest evidence for radial diffusion.

The first, and probably most widely quoted, observation of the inward movement of an energetic-electron flux profile was that reported for the period following the magnetic storm of 17—18 December 1962. The flux measurements of near-equatorial electrons ($E \gtrsim 1.6$ MeV) were made with a Type-302 Anton Geiger counter on the satellite Explorer 14, whose orbit is inclined by 33° to the earth's equatorial plane.

The flux profiles observed on several days following the storm are shown in Fig. 52a [111]. The inward radial movement of the "leading edge" of the electron distribution is clearly evident. An inward "velocity" $dL/dt \sim -0.04$/day at $L = 3.7$ is apparent in the data.

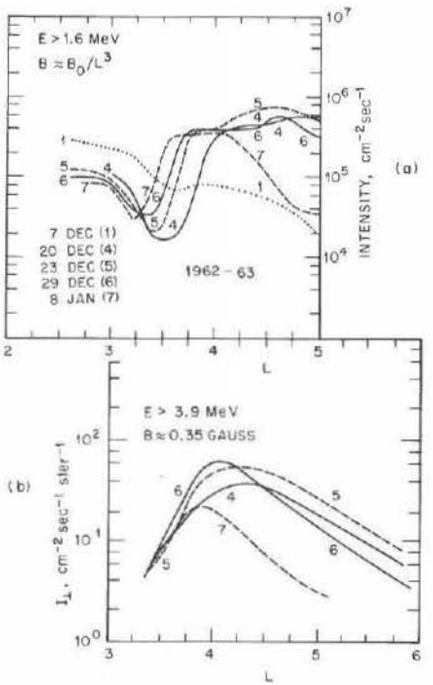

Fig. 52. Radial profiles of electron $I_{4\pi}$ [111] for $E > 1.6$ MeV near equator (a) and $I_\perp$ [112] for $E > 3.9$ MeV at low altitude (b), as observed on several days preceding and following the magnetic storm of 17 December 1962 (data from Explorer 14 and Alouette 1, respectively).

Plotted in Fig. 52b are the flux profiles of electrons ($E > 3.9$ MeV) detected during the same period from a shielded Type-302 Anton Geiger counter flown on the low-altitude satellite Alouette 1 [112]. The inward movement of the flux profiles measured on the low-altitude satellite

(Fig. 52b) is not as pronounced as that observed for particles mirroring closer to the equator. This observation perhaps confirms the theoretical prediction (see Section III.2) that radial diffusion caused by magnetic impulses will act primarily on particles that mirror near the equator.

A diffusion process known to conserve M and J, however, is not easily visualized in terms of constant-energy data as in Fig. 52. As indicated in the previous section, the phase-space distribution function $\bar{f}(M,J,L;t)$ should be plotted against L at selected intervals of time, with M and J held constant. Such a representation, however, requires information concerning the electron energy spectrum. Thus, data must be available from at least two (and preferably several) energy channels in the energy interval of interest.

The satellite Explorer 15 carried a pair of solid-state detectors able to measure the local unidirectional fluxes for $E>0.5$ MeV and $E>1.9$ MeV during the December 1962 event. Daily-median profiles of the $J=0$ fluxes are plotted in Fig. 53 [93] for the same days as in Fig. 52. It is quite evident from these Explorer-15 data that the lower-energy electron flux shows temporal variations dominated by a steady decay of intensity following the storm. In contrast, the higher-energy flux exhibits the inward movement of a "leading edge" of the flux profile apparent in Fig. 52a. It is clear, then, that an adequate analysis of these data entails a thorough consideration of both of these superficially disparate observations. The first step in such an analysis is to present the data in the form of $\bar{f}(L,t)$ at constant M and J.

For equatorially mirroring ($J=0$) particles, as represented in Fig. 53, the transformation from flux to $\bar{f}(L,t)$ is simplified by the fact that $\bar{f}=(1/2m_0MB_0)L^3\bar{J}_\perp$. The energy corresponding to each value of M is determined as a function of L from (2.07). The *differential* flux $J_\perp$ at each L-dependent energy is deduced by fitting a suitable spectral form (typically exponential or power-law) between the two measured (daily median) *integral*-flux values $I_\perp$ (*cf.* Fig. 53). Results of this interpolation are illustrated in Fig. 54 [93]. No "crest" is evident in the distribution function $\bar{f}(L,t)$ between $L=3.4$ and $L=4.8$; the particles in Fig. 54 appear to be diffusing inward from a source beyond $L\sim 5$. The superimposed decay (*cf.* Fig. 39, Section IV.3) appears to be greater at $M=300$ MeV/gauss than at $M=750$ MeV/gauss, and so the inward diffusion of $\bar{f}(L,t)$ at the lower M value is obscured. Quantitative procedures for extracting D_{LL} and τ from the data in this format are described in Chapter V.

A number of subsequent measurements showing an apparent inward movement of the "leading edge" of an electron-flux profile have been reported by various investigators. The data shown in Fig. 55 were obtained on the satellite Elektron 3 in September 1964 [94]. The fluxes

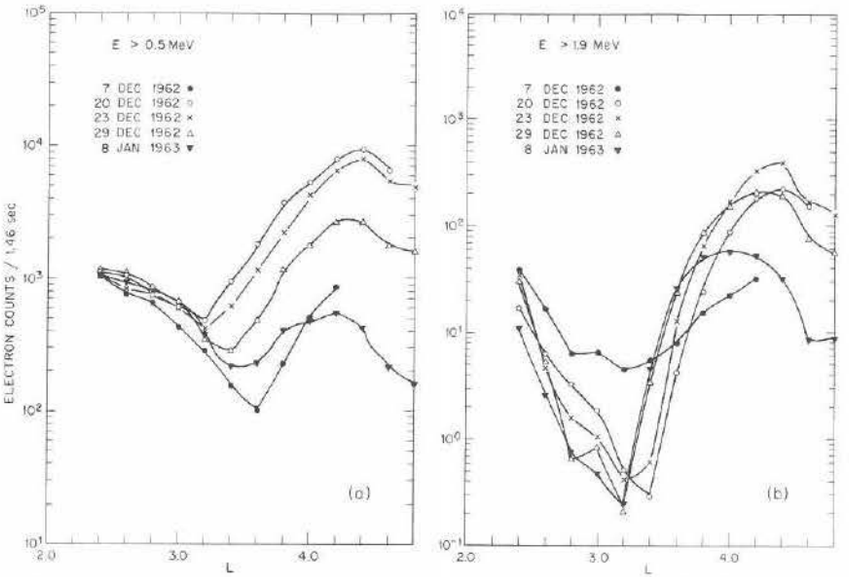

Fig. 53. Daily-median intensities of equatorially mirroring electrons [93] observed on Explorer 15 before and after the magnetic storm of 17 December 1962 (*cf.* Fig. 52).

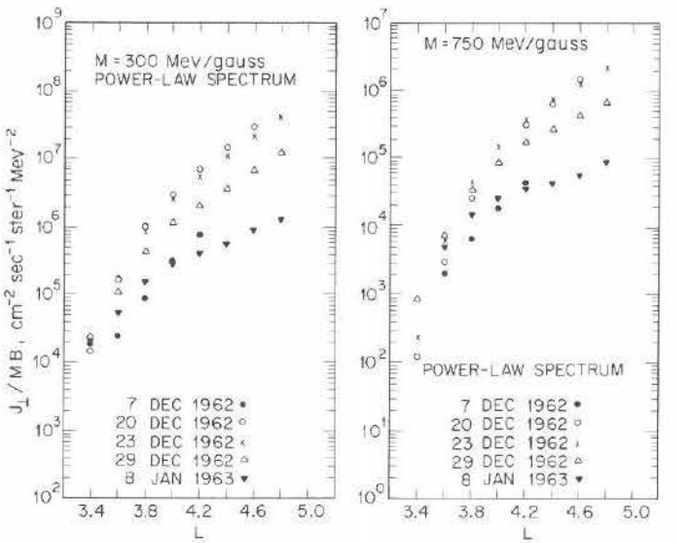

Fig. 54. Electron distribution functions ($\times 2m_0$) at $J=0$, as deduced from Fig. 53 and calibration data by assuming a power-law spectrum for energy interpolation [93].

labeled VS-1 are electrons of energy $E>100\,\text{keV}$ and were measured with a shielded gas-discharge counter; the fluxes labeled VF-1 are electrons of energy $E>400\,\text{keV}$ and were measured with a shielded NaI(Tl) crystal attached to a phototube. Inward movement of the "leading edge" in Fig. 55 is much less evident at $E\sim100\,\text{keV}$ than at $E\sim400\,\text{keV}$. This comparison is not surprising in view of Fig. 53, where inward movement is not apparent even at $E\sim500\,\text{keV}$. Conditions in the radiation belts must have been different in September 1964 from those in December 1962 in order to permit detection of the apparent inward movement at $E\sim400\,\text{keV}$. The 400-keV channel in Fig. 55 exhibits an apparent "leading-edge velocity" $dL/dt\sim-0.2/\text{day}$ at $L\approx4.4$; as in the December 1962 event, a quantitative interpretation of the underlying dynamics would require the data to be converted to a distribution function at constant M and J.

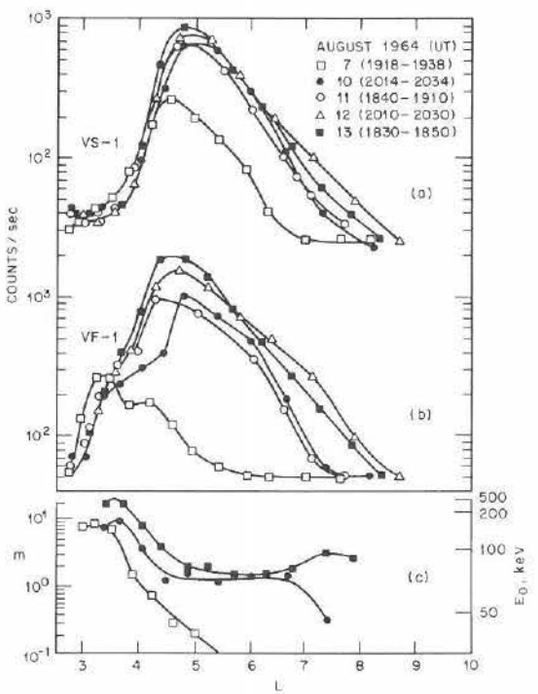

Fig. 55. Electron-intensity profiles observed in two energy channels (VS-1, $E>100\,\text{keV}$; VF-1, $E>400\,\text{keV}$) on Elektron 3 during August 1964, with spectral indices $m\equiv(-d\ln J_{4\pi}/d\ln E)$ and $E_0=(-d\ln J_{4\pi}/dE)^{-1}$ deduced from ratio of counting rates [94].

Storm-associated enhancements of inner-zone electron fluxes became apparent beginning in mid-1966, by which time the artificial belts created by high-altitude nuclear detonations no longer significantly contaminated the inner zone (see Section IV.2). Electrons naturally "injected" at $L\sim2$ subsequently appear to diffuse deeper into the inner zone. An example of the apparent inward movement of naturally "injected" electrons following the magnetic storm on 2 September 1966 is shown in Fig. 56 [95]. These data were obtained by a magnetic spectrometer

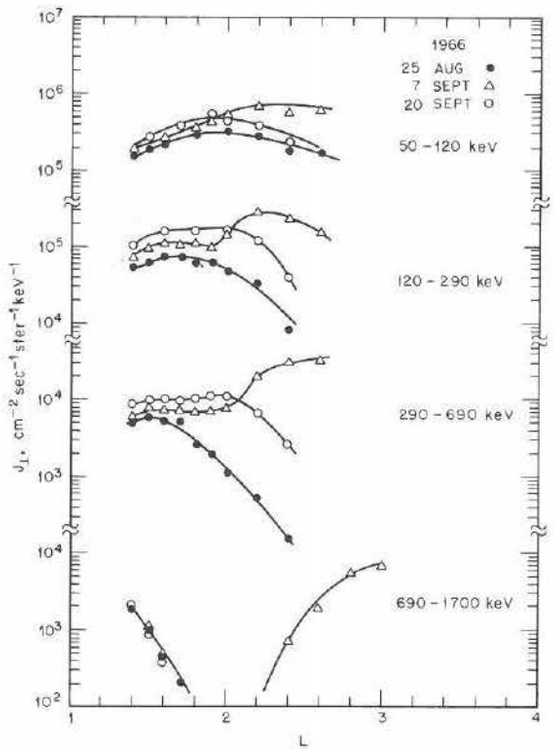

Fig. 56. Inner-zone electron-flux profiles observed on OGO 3 before and after the large magnetic storm of 2 September 1966 [95].

flown on the OGO-3 satellite. Electron fluxes were enhanced at all observed energies and L values in consequence of the September 1966 storm. The largest enhancements appeared in the interval between $L\approx2.0$ and $L\approx2.4$. On the eighteenth day after the storm the electron intensities at the lower L values were continuing to increase, while the original enhancements at $L\approx2.0$—2.4 had disappeared.

It is essentially impossible to identify a "leading-edge velocity" in Fig. 56, but a "crest velocity" $dL_c/dt \approx -0.04$/day can perhaps be deduced at 50—120 keV. This "velocity" should be assigned to the median L_c value ($L \approx 2.1$) at which $(\partial J_\perp/\partial L)_E = 0$ for the interval 7—20 September 1966. Following a similar "injection" during the magnetic storm of 25 May 1967, the "crest" of a flux profile ($E > 0.5$ MeV) was observed to move such that $dL_c/dt \approx -0.02$/day between $L \approx 1.9$ and $L \approx 1.25$ [96].

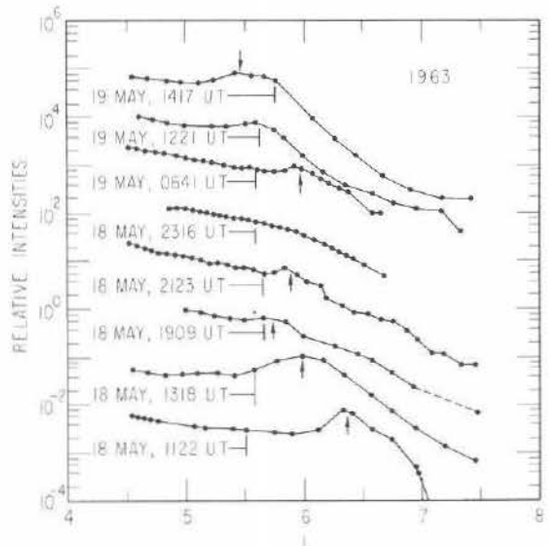

Fig. 57. Profiles of outer-zone electron flux ($E > 1.6$ MeV, omnidirectional) measured on Injun 3 during May 1963 [97]. Arrows denote instantaneous position of inward-moving "crest" (secondary maximum). Ordinate is separately normalized for each profile.

Typical "crest velocities" in the *outer* zone may be deduced from Fig. 57, which contains a selected interval of Injun-3 electron data ($E > 1.6$ MeV) obtained with a Type-302 Geiger tube [97]. Various secondary maxima of the integral flux appear to move inward with time, with a velocity $dL_c/dt \approx -10^{-2}\,(L/4)^8$ day^{-1}. This is about half the value typically deduced for a "leading-edge velocity" (see Fig. 52a). The dynamical significance of "velocities" obtained from such constant-energy data is somewhat dubious, although studies of this type have played an important historical role in radiation-belt phenomenology.

For the quantitative analysis of diffusion phenomena, natural electron "injection" events have the disadvantage of introducing spatially broad flux profiles, for which the competing dynamical processes are difficult to isolate. On the other hand, several of the artificial radiation belts created by high-altitude nuclear detonations were initially confined to rather narrow L ranges. Figure 58, for example, illustrates the evolution

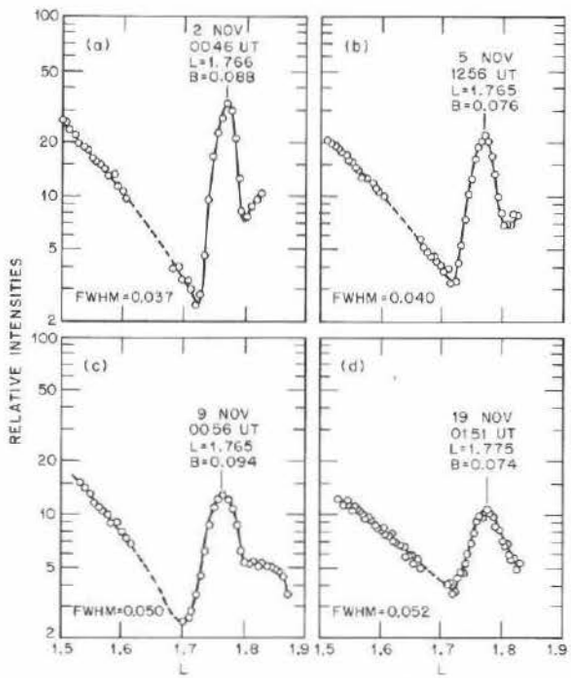

Fig. 58. Evolution of inner-zone electron-flux profile ($E > 1.9$ MeV, omnidirectional) observed on Explorer 15 following high-altitude nuclear explosion of 1 November 1962 [75].

of an electron-flux profile ($E > 1.9$ MeV) measured by an omnidirectional solid-state detector aboard the satellite Explorer 15 [75]. The narrow "spike" of electron flux centered at $L \approx 1.77$ had been injected by the Soviet high-altitude explosion of 1 November 1962. The full widths at half maximum (FWHM) were evaluated by fitting a Gaussian profile to each individual peak after subtracting the extrapolated background of Starfish-produced electrons (see Section IV.2). No systematic temporal shift in the position of the peak is apparent. The phenomenon of radial diffusion is evident, however, in the broadening of the flux profile with time. The value of (FWHM)^2 appears to increase at a rate $\sim 7 \times 10^{-5}$

day^{-1}. If the indicated radial diffusion preserved particle energy rather than M and J, this numerical result could be translated[37] into a radial-diffusion coefficient $D_{LL} \sim 6 \times 10^{-6}$ day^{-1} [see (2.20)—(2.23), Section II.3].

The broadening of the profile contributed very little to the observed decrease in the trapped electron flux at $L \approx 1.77$. During the time span of the data plotted in Fig. 58, the maximum intensity decreased by a factor of approximately four, while the width increased by only $\sim 30\%$. Thus, a loss mechanism clearly must have been operating simultaneously with radial diffusion to account for the remaining decay (factor of 4/1.3) during the 17-day interval. The associated e-folding time (~ 15 days) is somewhat shorter than would have been expected from Fig. 41 (Section IV.3), in view of the fact that 1.9-MeV electrons in the outer zone are known to decay more *slowly* than 0.5-MeV electrons.

The 15-day lifetime deduced from Fig. 58 corresponds to $D_{xx} \approx 0.01$ day^{-1} (see Section II.7). If this pitch-angle diffusion coefficient is inserted in (3.40) or (3.45), however, the resulting radial-diffusion coefficient at $L \approx 1.77$ cannot exceed $\sim 8 \times 10^{-7}$ day^{-1} outside the loss cone (see Fig. 30, Section III.7). Shell splitting thus fails by a factor ~ 7 to account for the radial diffusion illustrated in Fig. 58. In the absence of other known radial-diffusion mechanisms that preserve E, it seems likely that the data should be analyzed at constant M and J (see Section V.6).

IV.7 Fluctuating Magnetospheric Fields

Compared with the extensive spatial and spectral measurements of the trapped electron and proton populations, the observation of wavelike electric- and magnetic-field fluctuations (plasma turbulence) in the magnetosphere remains in the basic exploratory stage. Of the wavelike phenomena that have been observed, most are related to pitch-angle diffusion rather than radial diffusion. The disturbances known to produce significant radial diffusion often extend coherently over the entire magnetosphere (see Sections III.2 and III.3) and so it may be inappropriate to characterize them as waves.

As indicated in Section II.5, electromagnetic waves propagating in the whistler mode are in the correct frequency band to cyclotron-resonate with radiation-belt electrons. All the various types of VLF signals that

[37] Division of the time derivative of (FWHM)^2 by $16 \ln 2$ yields a radial diffusion coefficient compatible with (3.42). For a profile as narrow as that in Fig. 58, it is safe to neglect the term $L^{-2}[\partial(L^2 D_{LL})/\partial L](\partial \bar{f}/\partial L)_{E,x}$ in the expansion of (3.42).

propagate in the whistler mode (*e.g.*, chorus, hiss, hooks, and whistlers) can in principle produce pitch-angle diffusion, and it appears from satellite VLF data that only a small fraction of the measured VLF energy belongs to whistlers generated by lightning strokes (see Section II.3). Most of the wave energy is of magnetospheric origin.

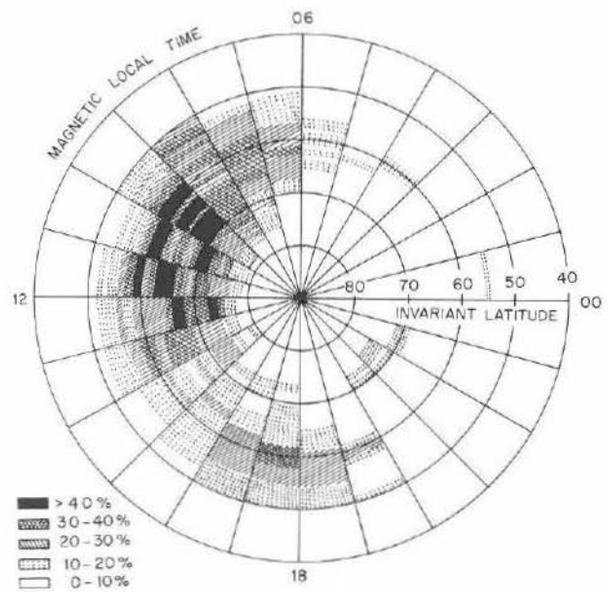

Fig. 59. Probability-of-occurrence distribution for wide-band VLF noise (0.2—7.0 kHz) with magnetic amplitude $> 1.8 m\gamma$ rms (root-mean-square), based on Injun-3 observations at altitudes up to 2700 km [98].

Calculations have shown that root-mean-square (rms) magnetic-field fluctuations $\sim 1 m\gamma$ in the frequency range of whistler-mode disturbances would be sufficient to account for the lifetimes shown in Fig. 41 for electrons that mirror at magnetic latitudes $\gtrsim 20°$ [43]. Noise of this magnitude is a common occurrence at altitudes up to ~ 2700 km in the invariant-latitude[38] range 50°—70°. The probability-of-occurrence distribution for VLF signals ($\gtrsim 1.8 m\gamma$) in the 0.2—7.0 kHz band, as measured on the Injun-3 satellite, is shown in Fig. 59 [98]. The VLF

[38] Low-altitude satellite data are frequently organized with respect to invariant magnetic latitude Λ, defined such that $L_m = \sec^2 \Lambda$. The invariant latitude of a field line is the magnetic latitude at which the line would intersect the earth's surface in a centered-dipole idealization.

noise drops off sharply below $\Lambda \sim 50^\circ$ ($L \sim 2.5$) and is also largely absent in the quadrant centered on midnight. The drop-off in disturbance below $\Lambda \sim 50^\circ$ may account for the reduced electron loss rates (longer lifetimes) found at the lower L values (see Fig. 41).

Measurements of energetic electrons (300 keV to 2.3 MeV) reveal a pronounced peak in the profile of precipitating outer-zone electrons [99]. The location of this peak is strongly correlated in L with the morningside location of the plasmapause (see Section I.6). Further, the morningside location of the plasmapause is observed to correlate well with the occurrence of ELF emissions. Apparently the most intense pitch-angle diffusion of electrons into the loss-cone ($x_b > x > x_c$) is that produced by the ELF emissions on the morning side of the magnetosphere. The electrons subsequently drift in longitude to the South Atlantic "anomaly" where they enter the atmosphere and are lost from the radiation belts.

In view of the coincidence in frequency, the Pc-4 ($\sim 10^{-2}$ Hz) micropulsation observed at ATS 1 and shown in Fig. 18d (Section II.3) may resonate with the bounce motion of ring-current protons (~ 15 keV). At synchronous altitude, the wave was seen only in the ζ (compressional) component. Spectral analyses of $\dot{\mathbf{B}}$ at ATS 1 and at College, Alaska, during this event are shown in Fig. 60 [100]. At College (which lies near the foot of the ATS-1 field line) the oscillation was almost entirely noncompressional. The relative spectral intensities suggest a 2% efficiency of mode conversion from an apparent magnetosonic wave at the equator (see Section II.5) to a transverse Alfvén wave [see (2.51b) Section II.6] in the lower ionosphere.

For other disturbances, notably sudden impulses (*si*) and sudden commencements (*sc*), the magnetic-field perturbation seen on the ground is similar in magnitude to that seen in the magnetosphere at synchronous altitude[39]. The factor relating such field perturbations seen on the ground and at ATS 1 is often compatible with that suggested in Fig. 9 (from the induced-dipole effect, Section I.5). Thus, a sudden impulse in b [equation (1.45), Section I.5] ideally produces

$$\dot{\mathbf{B}} \approx \hat{\theta}(\dot{b}/b)(a/b)^3[3B_1 - 4B_2(r/b)\cos\varphi] \tag{4.02a}$$

at the satellite ($r = 6.6a$, $\theta = \pi/2$) and

$$\dot{\mathbf{B}} \approx \hat{\theta}(\dot{b}/b)(a/b)^3(9B_1/2)\sin\theta \tag{4.02b}$$

on the ground ($r = a$). The φ dependence of $\mathbf{B}$ on the ground should be negligible, according to (1.45). The addition of a conducting earth

[39] An *sc* is followed by the main phase of a magnetic storm, while an *si* is not.

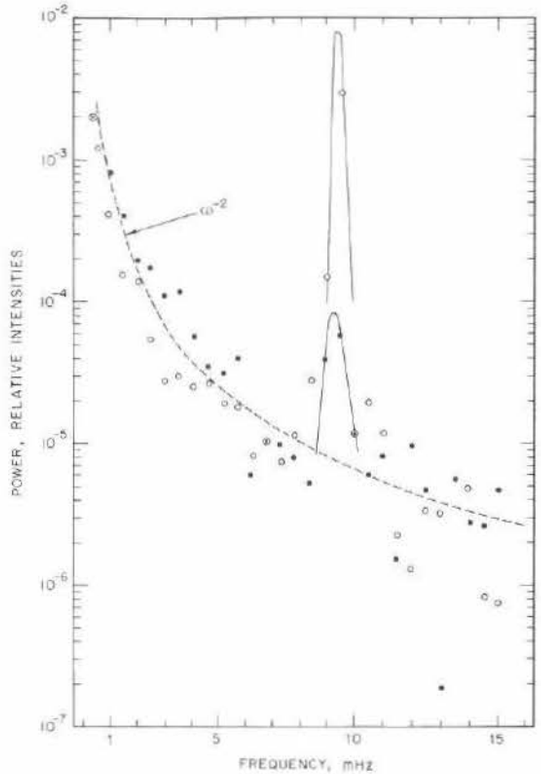

Fig. 60. Relative spectral densities of $\dot{\mathbf{B}}$, *i.e.*, contributions to $\langle \dot{\mathbf{B}}^2 \rangle$ per unit frequency interval, at ATS 1 (open circles) and College (filled circles) during Pc-4 event shown in Fig. 18d [100]. Solid curves schematically trace central peak of each spectrum. Dashed curve represents inverse-square background common to both spectra.

[in (4.02b)] makes $\dot{B}_r$ vanish at $r = a$. In this idealization, temporal variations of $\mathbf{B}$ are excluded (on a sudden-impulse time scale) from the region $r < a$.

The magnetic spectral density $\mathscr{B}_z(\omega/2\pi)$ required in (3.13) is thus related to $\mathscr{B}_0(\omega/2\pi)$, as observed on the ground, by the simple transformation

$$\mathscr{B}_0(\omega/2\pi) \approx (9/4)\sin^2\theta\, \mathscr{B}_z(\omega/2\pi). \tag{4.03}$$

If extraneous disturbances seen on the ground but not at the satellite (*e.g.*, resulting from currents localized in the ionosphere) are excluded from the spectrum by a careful search of the magnetograms for *si*'s

and *sc*'s, it becomes possible to estimate the magnitude of D_{LL} due to the occurrence of these *si*'s and *sc*'s. By analogy with (3.20), the ground-based observations yield a spectral density

$$\mathscr{B}_0(\omega/2\pi) = \frac{2(\tau_d^2/\tau)\Sigma(\Delta B_0)^2}{1+\omega^2\tau_d^2}, \tag{4.04}$$

which reduces to $\mathscr{B}_0(\omega/2\pi) \approx (2/\omega^2\tau)\Sigma(\Delta B_0)^2$ in the limit $\omega^2\tau_d^2 \gg 1$, *i.e.*, for drift periods short compared to the characteristic decay time of an impulse.

A four-year compilation of equivalent equatorial ($\theta = \pi/2$) data obtained from ground-based measurements is summarized in Table 10 [101]. If the probability of *sc* and *si* occurrence (per year) is multiplied by the product of the impulse-amplitude bin limits, the sum over all amplitude bins yields the estimate that $(1/\tau)\Sigma(\Delta B_0)^2 \approx 5.11 \times 10^4 \gamma^2/\text{yr} \approx 140\gamma^2/\text{day}$. For $\omega^2\tau_d^2 \gg 1$, the *sc*'s and *si*'s thus apparently produce a radial-diffusion coefficient[40]

$$D_{LL} \approx 10^{-8}(a/b)^2 L^{10}\,\text{day}^{-1} \approx 10^{-10} L^{10}\,\text{day}^{-1} \tag{4.05}$$

for $b = 10a$ and $\gamma = 1$ [see (3.14), Section III.2].

Table 10. Summary of Magnetic Impulses (1958—61)

Amplitude	Frequency	Contribution to $(10/L)^{10} D_{LL}$, day^{-1}	
$\Delta B_0, \gamma$	Events/yr	Quasilinear	Nonlinear
>100	0.5	0.17	0.25
60—99	1.8	0.20	0.31
40—60	2.3	0.10	0.12
20—40	21.	0.32	0.36
5—20	61.	0.16	0.16
~ 2	720.	0.05	0.05
Total	~ 800	1.00	1.25

Compiling a list such as Table 10 requires subjective judgements, and different investigators often disagree on the results. Values of D_{LL} ranging from 2—$4 \times 10^{-11} L^{10}\text{day}^{-1}$ (considering only *sc*'s [102]) up to 4—$13 \times 10^{-9} L^{10}\text{day}^{-1}$ (both *sc*'s and *si*'s [103]) have been reported[41].

[40] This is the "quasilinear" result. The "nonlinear" result (last column) is inferred from the published results of a nonlinear calculation [101] by requiring agreement with "quasilinear" theory for the smallest impulses.

[41] The estimate of 4—$13 \times 10^{-9} L^{10}\text{day}^{-1}$ was based upon a summary of sudden-impulse data from Explorer 12 as well as from ground-based records.

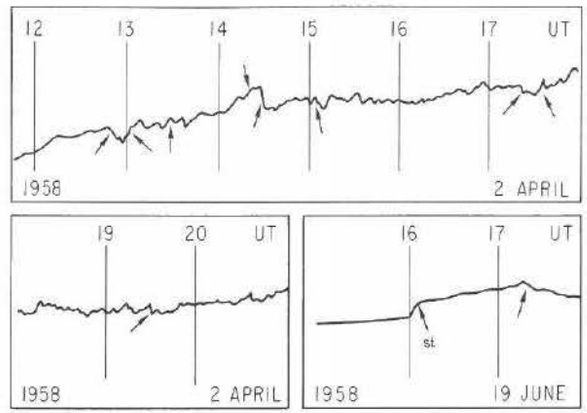

Fig. 61. Horizontal (H) component of magnetic records from Honolulu Observatory, showing sudden impulse (*si*) recognized in official compilations of such data [105] and similar fluctuations (unlabeled arrows) not present on enough other magnetograms in the global network to qualify as recognized sudden impulses [104].

Values up to $2 \times 10^{-10} L^{10}\text{day}^{-1}$ can be obtained in place of (4.05) by slightly modifying the manipulation of the data of Table 10 [101].

Part of the subjectivity involved in the inspection of ground-based magnetometer records is illustrated in Fig. 61 [104]. Several features (designated by arrows) certainly look like sudden impulses, but only one (that labeled *si*) is officially recognized as such in compilations of geomagnetic and solar data [105]. In the absence of any apparent morphological distinctions, it would seem that all events in Fig. 61 should be included in (4.04). This apparently has not been done in Table 10, which lists only about 800 events per year. Moreover, many of the events designated by arrows in Fig. 61 have rise times τ_r and decay times τ_d that do not fit the pattern $\tau_r \ll 2\pi/\Omega_3 \ll \tau_d$, where $2\pi/\Omega_3$ is the azimuthal-drift period of a radiation-belt particle. Such impulses will alter the functional form of $\mathscr{B}_0(\omega/2\pi)$, causing it to deviate (at high and low frequencies) from proportionality to ω^{-2}. The radial-diffusion coefficient is accordingly reduced for particles having $\Omega_3^2\tau_r^2 \gtrsim 1$, just as (4.04) suggests a reduction from (4.05) for $\Omega_3^2\tau_d^2 \lesssim 1$. In evaluating expressions for D_{LL} in such cases, it is convenient to recall [*cf.* (1.35), Section I.4] that

$$|2\pi/\Omega_3| = (m_e/m_0)(\gamma/L)(\gamma^2-1)^{-1} \times 173.2\,\text{min} \tag{4.06}$$

at $\gamma = 1$ in the dipole field ($173.2 \approx 100/\sqrt{3}$).

One way to avoid the subjectivity of visually identifying *sc*'s and *si*'s is to generate, directly from digitized magnetograms, a power spectrum of the field variations. The result of such an analysis of data obtained on the ground at $L \approx 2.7$ is shown in Fig. 62 [106] and corresponds to an equatorial spectrum

$$\mathscr{B}_\theta(\omega/2\pi) \approx 1.0 \times 10^{-2}[(2\pi/\omega) \div 1\,\text{sec}]^2\,\gamma^2/\text{Hz} \qquad (4.07)$$

at frequencies $\omega/2\pi \lesssim 40$ mHz. According to (4.03) and (3.14), the spectrum yields a radial-diffusion coefficient

$$D_{LL} \approx 1.2 \times 10^{-8} L^{10}\,\text{day}^{-1} \qquad (4.08)$$

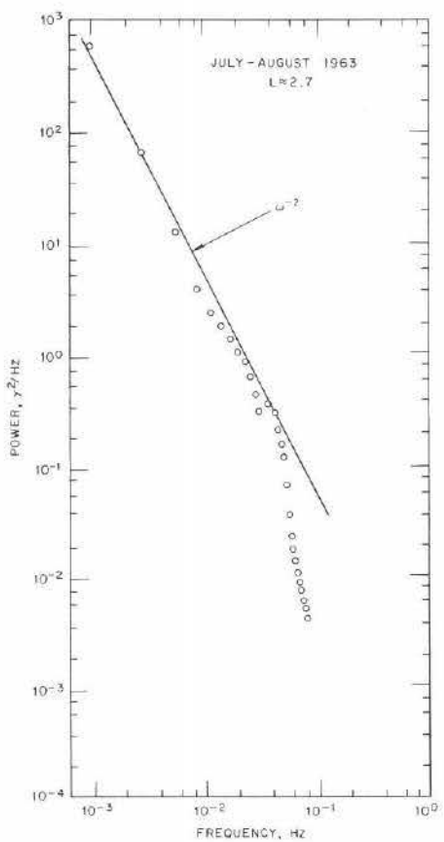

Fig. 62. Spectral density (1—200 mHz) of fluctuations in total field intensity B observed at Lebanon State Forest, New Jersey. Compilation includes all available data, regardless of local time or K_p index [106].

for equatorially mirroring particles (assuming $b = 10a$). This number is compatible with the maximum value ($\sim 13 \times 10^{-9} L^{10}\,\text{day}^{-1}$, see above) reported by an investigator using *sc*'s and *si*'s, but is slightly large compared to the *total* D_{LL} that outer-zone particle observations appear to require (see Chapter V). The result given by (4.08) is ~ 100 times that given by (4.05) for what is alleged to be the same diffusion mechanism, *viz.*, the violation of Φ by sudden *magnetic* perturbations.

Part of the disagreement[42] that is noted among results differently obtained [*cf.* (4.05) and following discussion] may arise from the production of ionospheric currents by impulses that are *electrostatic* in the magnetosphere. These currents would cause **B**-field perturbations that are detectable on the ground (*cf.* Fig. 61) but insignificant in the outer zone. Another possibility is that magnetic-field perturbations in space are magnified by induced ionospheric currents to yield an enhancement on the ground that far exceeds the factor $\sim 3/2$ implied by (4.02). Such an effect may help to account for the fact that the *diurnal* variation of **B** at the earth's surface during quiet periods is ~ 10 times the amplitude $\sim 2\gamma$ predicted [28] by (1.45).

According to (4.02) a sudden magnetic impulse should have a nearly φ-independent amplitude at the ground, but a strongly φ-dependent amplitude (larger at noon than at midnight) in the vicinity of synchronous altitude. Comparisons of sudden-impulse amplitudes observed at ATS 1 and on the ground at Honolulu (*cf.* Section III.1) sometimes confirm this expected diurnal variation of their ratio, while at other times such comparisons are inconclusive [107]. As suggested above, the ionosphere (which is, on the average, a much better conductor by day than at night) may play a role that is not yet understood.

The results indicated by (4.05) and (4.08) are thus subject to the considerable uncertainties that often surround the quantitative application of ground-based observations to magnetospheric phenomena. Table 10 covers a period of moderate solar and geomagnetic activity, and the consequent D_{LL} given by (4.05) would perhaps have been larger at solar maximum and smaller at solar minimum (*cf.* Fig. 51, Section IV.5). The data for Fig. 62 cover only a few selected days in 1963 and do not represent a true average of any sort. It is difficult in any case to reconcile the disparate values of D_{LL} indicated by (4.05) and (4.08).

For several of the larger impulses listed in Table 10, the "quasilinear" analysis leading to (3.13) could easily be inadequate. A pair of radiation belt particles initially coincident in L (~ 5) but 180° out of phase in

[42] Aside from obvious considerations, such as the fact that the various data were acquired during different time periods.

drift could easily find themselves separated by $\Delta L \gtrsim 1$ following an impulse $\gtrsim 50\gamma$ in amplitude [*cf.* (3.11)]. Moreover, a random succession of such large impulses may violate (3.13) to some extent, by virtue of a nonlinearity in the relationship among L, dL/dt, and db/dt [*cf.* (3.12), Section III.2]. As a consequence of this nonlinearity, the radial-diffusion coefficient implied by the data of Table 10 is probably somewhat larger than (4.05) indicates, and the relative contribution of the larger impulses is somewhat enhanced (see Table 10, last column) [101].

IV.8 Drift Echoes

As noted in Section III.1, magnetic sudden impulses are frequently followed by drift-periodic echoes in the outer-zone particle fluxes. Figure 23 (Section III.1) illustrated this phenomenon for unidirectional ($\approx J_\perp$) electron fluxes at synchronous altitude. In Fig. 63, drift echoes are observed in the fluxes measured by the same seven unidirectional electron channels on the ATS-1 satellite [108]. The characteristic echo frequency observed in each distinctly echoing channel of Fig. 63 is plotted (Fig. 64) against the value of $(\gamma^2-1)/\gamma$ corresponding to the respective nominal electron energy. The resulting linear relationship (with a reasonable

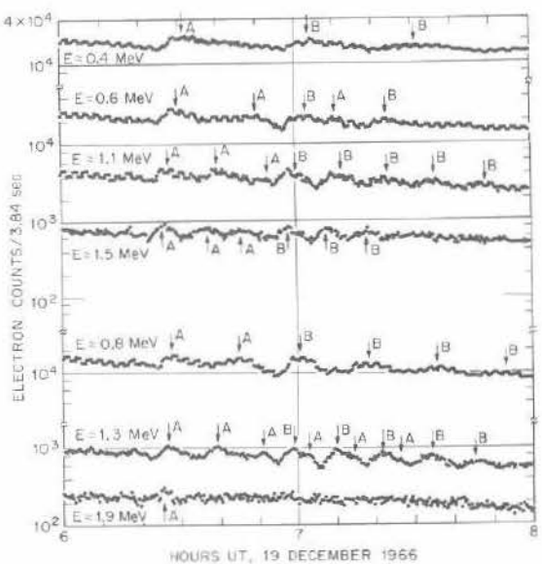

Fig. 63. Unidirectional electron fluxes (roughly $J_\perp$ channels) measured on ATS 1 during period of overlapping drift-echo events, denoted *A* and *B* [108].

magnitude for Ω_3, as shown below) confirms the drift-periodicity of the echoes[43]. If $J_\perp$ is proportional to E^{-l} on the drift shell in question (*cf.* Section II.6), the typical spread in Ω_3 may be estimated as $\Delta\Omega_3 \sim \Omega_3/l$ for a given broad energy channel. The drift-echo amplitude therefore decays with an *e*-folding time $\sim l/\Omega_3$ ($\sim l/2\pi$ drift periods) by virtue of phase mixing in φ_3 among particles detected in the same energy channel (see Sections II.1 and III.1).

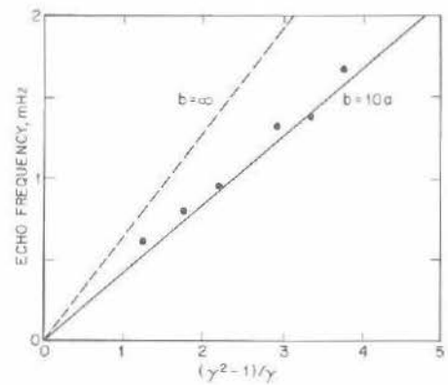

Fig. 64. Empirical drift-echo frequencies (filled circles) from Fig. 63 for nominal electron energies $E=(\gamma-1)m_0c^2$. Theoretically expected drift frequencies for pure-dipole field (dashed line) and compressed-dipole field (solid line) are derived from (4.09).

The magnitude of Ω_3 in Fig. 64 is smaller than would be expected in a dipole field ($b=\infty$) for the same electron energy and drift-shell radius. For equatorially mirroring particles the magnetospheric compression represented by B_1 in (1.45) acts to reduce the angular drift velocity. If B_2 is neglected altogether in (1.45), the equatorially mirroring particle sees a guiding-center force [*cf.* (3.32)] equal to $-(M/\gamma)(\partial B/\partial r)$ in the radial direction. The resulting azimuthal drift is such that

$$\begin{aligned}\Omega_3 &= v_d/r = (c/qBr)(M/\gamma)(\partial B/\partial r)\\ &= -3B_0(m_0c/2qB^2\gamma)(\gamma^2-1)(c/a)^2(a/r)^5\,. \qquad (4.09)\end{aligned}$$

[43]The dependence of Ω_3 on γ is very weak (*cf.* Fig. 7) and can be neglected here, even if the form of the pitch-angle distribution varies with electron energy. The threshold energy is regarded as the nominal energy of particles that count in a given channel. If the energy spectrum were oddly shaped, or the threshold energy difficult to identify from the detector counting-efficiency curves $\varepsilon_j(E)$, it might be necessary to plot the function $J_\perp(E)(dE/d\Omega_3)\varepsilon_j(E)$ against $(\gamma^2-1)/\gamma$ for each energy channel (j) in order to identify the mean (or most probable) drift frequency and relative bandwidth.

where $B=B_0(a/r)^3+B_1(a/b)^3$. The drift frequency expected from (4.09) is found to agree well with that observed in each energy channel (Fig. 64). Moreover, equation (4.09) clearly predicts that $(\partial\Omega_3/\partial r)_E=0$ at $r=(B_0/5B_1)^{1/3}b\approx(\pi/5)b\approx 6.3a$, *i.e.*, at $B=6B_1(a/b)^3\approx 150\gamma$, if $b=10a$. Thus, the drift frequency of a particle having $y=1$ and a fixed energy attains its maximum with respect to r at a location $\sim 0.3a$ below synchronous altitude[44].

Drift echoes are produced because a sudden impulse differentially (with respect to φ_3) changes the energy and L value of a population of trapped particles. In other words, the magnitudes of ΔE and ΔL depend upon a particle's drift phase at the instant of the impulse (see Fig. 65) [55]. The effect of magnetic impulses on a particle population having $J=0$ can be estimated by referring to the model in Section III.2.

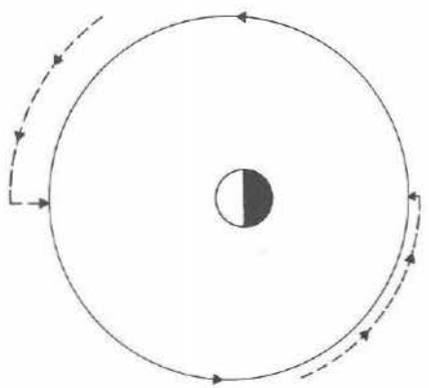

Fig. 65. Schematic illustration of third-invariant violation by sudden compression of magnetosphere. Electrons initially on different drift paths (dashed curves) are accidentally 180° apart in drift phase at time of compression that puts them both onto the same, new drift shell. The mean inward displacement and energization is adiabatic, related to the global increase in $B_1(a/b)^3$. The particle energized on the day side has thus moved inward in L, while the particle less energized on the night side has moved outward in L, as defined by (1.37).

The equatorial **B** field seen by a particle in the magnetic-field model specified by (1.45) points in the $-\hat{\boldsymbol{\theta}}\,(=+\hat{\mathbf{z}})$ direction and has a magnitude

$$B_e(r,\varphi;t)=B_0(a/r)^3+B_1(a/b)^3-B_2(a/b)^3(r/b)\cos\varphi\,. \qquad (4.10)$$

[44]The accuracy of (4.09) is perturbed only to *second* order in B_2 if the azimuthal asymmetry of **B** is included in the calculation of Ω_3.

According to Table 7 (Section III.2), a magnetic impulse induces an electric field

$$E_\varphi(r,\varphi;t)\approx(3/2c)(a/b)^3(db/dt)\{B_1(r/b) -(64/63)B_2(r/b)^2[1+(13B_1/832B_0)(r/b)^3\cos\varphi] +(2B_2/63B_0)B_2(r/b)^6\cos 2\varphi\} \qquad (4.11\,a)$$

$$E_r(r,\varphi;t)\approx -(4/7c)(a/b)^3(db/dt)\{B_2(r/b)^2[1-(9B_1/52B_0)(r/b)^3]\sin\varphi -(7B_2/25B_0)B_2(r/b)^6\sin 2\varphi\} \qquad (4.11\,b)$$

in the equatorial plane ($\theta=\pi/2$) of this magnetic-field model.

For $db/dt=0$, an equatorially mirroring particle would follow a path of constant B, as given by (4.10). A sudden impulse (at time $t=t_0$) alters the value of B seen by the particle; the rate of change is given by

$$dB_e/dt=(\partial B_e/\partial t)+c(E_\varphi/B)(\partial B_e/\partial r)-c(E_r/rB_e)(\partial B_e/\partial\varphi) \approx -(3/b)(a/b)^3(db/dt)[(5/2)B_1-(20/7)B_2(r/b)\cos\varphi] \qquad (4.12)$$

to lowest order in ε_1 and ε_2 (see Section I.7). The resulting phase organization can be traced via Liouville's theorem (Section I.3). It can thus be shown that

$$\ln f(M,J,L_m(t_0^+),\varphi_3;t_0^+)-\ln\bar{f}(M,J,L_m(t_0^+);t_0^-) \approx\{1-(1/2\gamma)(\gamma+1)(\partial\ln\bar{J}_\perp/\partial\ln E)_L +(1/3)(\partial\ln\bar{J}_\perp/\partial\ln L_m)_E\}\ln[B_e(t_0^+)/B_e(t_0^-,\varphi_3)] \qquad (4.13)$$

for $J=0$, where $B_e=B_0/L_m^3$ (see Section I.5). For an impulse with vanishing rise time and small amplitude, it follows from (4.12) that

$$\ln[B_e(t_0^+)/B_e(t_0^-,\varphi_3)] \approx(5L_m^3/2B_0)[1-(8B_2/7B_1)(L_m a/b)\cos\varphi_3]\,\Delta[B_1(a/b)^3]\,, \qquad (4.14)$$

where the drift phase φ_3 is defined in terms of a particle's azimuthal coordinate φ at time $t=t_0$ (see Section I.5). Following the sudden impulse, as **B** remains constant in time, the evolution of $J_\perp\equiv p^2 f$ is given by

$$\ln J_\perp(E,x=0,L_m,\varphi;t)-\langle\ln J_\perp(E,x=0,L_m,\varphi_3)\rangle \approx\{1-[(\gamma+1)/2\gamma](\partial\ln\bar{J}_\perp/\partial\ln E)_L+(1/3)(\partial\ln\bar{J}_\perp/\partial\ln L_m)_E\} \times(-20L_m^4B_2/7B_1B_0)(a/b)\,\Delta[B_1(a/b)^3]\cos[\varphi-\Omega_3(t-t_0)]\,, \qquad (4.15)$$

where the angle brackets denote the drift average for $t>t_0$. Thus, as a result of the impulse at $t=t_0$, the spatial and spectral structure of

the previously ($t<t_0$) "unperturbed" magnetosphere unfolds in *time* as the representative particles subsequently drift past the satellite.

According to (4.15), the drift echoes observed at local noon ($\varphi=\pi$) will tend to have a smaller amplitude than those seen at local midnight ($\varphi=0$) because of the factor L_m^4. It follows that more events will escape detection when the satellite is at noon than when it is at midnight. A compilation of drift-echo events by probability of occurrence (Fig. 66) shows a diurnal variation having such an interpretation [109]. Here electron drift-echo events have been counted subject to the requirement that $\ln J_\perp$ "oscillates" with a peak-to-peak amplitude $\gtrsim 1/2$. Using a finer "resolution", $(\Delta \ln J_\perp)_{pp}\gtrsim 1/10$, it is possible to identify up to ~ 20 drift-echo events per day during periods of moderate geomagnetic activity.

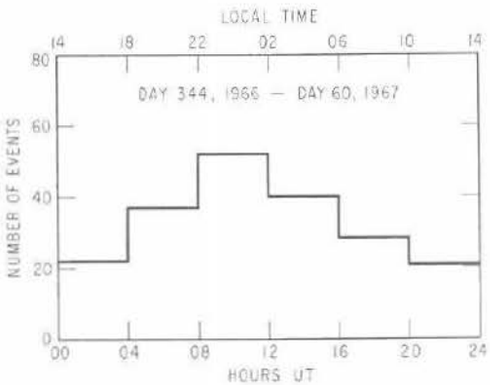

Fig. 66. Distribution of 200 major drift-echo events identified in ATS-1 electron data during an 82-day interval, in terms of satellite local time at beginning of event [109].

The compilation shown in Fig. 66 can be utilized, in principle, to estimate D_{LL} at synchronous altitude. If B_2 is tentatively neglected in order to simplify the field model [as in (4.09)] it can be shown without further approximation that

$$L\equiv 2\pi a^2 B_0 |\Phi|^{-1}=(r/a)\left[1-(B_1/2B_0)(r/b)^3\right]^{-1} \tag{4.16a}$$

$$L_m\equiv (B_0/B_e)^{1/3}=(r/a)\left[1+(B_1/B_0)(r/b)^3\right]^{-1/3}, \tag{4.16b}$$

where r is the equatorial drift-shell radius. At $r=6.6a$ it follows that $L=7.37$, $L_m=6.16$, and $dL/dL_m=1.93$. The radial-diffusion coefficient is thus given by

$$\begin{aligned} D_{LL}&=(dL/dL_m)^2(L_m^2/2\tau)\Sigma\langle(\Delta\ln L_m)^2\rangle\\ &=(dL/dL_m)^2(L_m^2/18\tau)\Sigma\langle(\Delta\ln B_e)^2\rangle\\ &=(dL/dL_m)^2(L_m^2/144\tau)\Sigma(\Delta\ln B_e)_{pp}^2\\ &=(dL/dL_m)^2(L_m^2/144\tau)\Sigma(\Delta\ln J_\perp)_{pp}^2\\ &\quad\div\{1-[(\gamma+1)/2\gamma](\partial\ln\bar J_\perp/\partial\ln E)_L-(\partial\ln\bar J_\perp/\partial\ln B_e)_E\}^2, \end{aligned} \tag{4.17}$$

where pp denotes the peak-to-peak amplitude.

The term $-(\partial\ln\bar J_\perp/\partial\ln B_e)_E$ in (4.17) is identical with the term $+(1/3)(\partial\ln\bar J_\perp/\partial\ln L_m)_E$ in (4.13) and (4.15). It can be estimated as ranging from ~ 2 at $E=0.4$ MeV to ~ 6 at $E=1.5$ MeV by measuring the diurnal variation of the electron fluxes at synchronous altitude on a sufficiently quiet day. A synchronous satellite measures a smaller flux in each *energy* channel at midnight than at noon (see Fig. 50, Section IV.5) because L_m is larger at midnight than at noon [6.39 *vs* 5.95, according to (4.10)]. The spectral index $-(\partial\ln\bar J_\perp/\partial\ln E)_L$ also shows a variation with energy for outer-zone electrons (~ 1 at $E=0.4$ MeV to ~ 5 at $E=1.5$ MeV). The divisor of $(\Delta\ln J_\perp)_{pp}^2$ in (4.17) is therefore of order unity[45], indicating that $\Delta\ln J_\perp$ (as seen by the observer) is roughly equal to $\Delta\ln B_e$ (as seen by a particle with $\varphi_3\sim\pi$). According to (4.12), the value of dB_e/dt is 4.6 times as large for $\varphi_3=\pi$ as for $\varphi_3=0$; strictly speaking, $(\Delta\ln B_e)_{pp}$ is the *difference* between the change in $\ln B_e$ experienced by a particle at noon and that seen by a particle at midnight.

Figure 66 indicates an average of two drift-echo events per day for which $(\Delta\ln J_\perp)_{pp}\gtrsim 1/2$. As some events have amplitudes larger than the nominal threshold, the estimate that $(1/\tau)\Sigma(\Delta\ln J_\perp)_{pp}^2\sim 1\,\text{day}^{-1}$ appears reasonable. It then follows from (4.17) that $D_{LL}\sim 1\,\text{day}^{-1}$ $\sim 10^{-9}L^{10}\,\text{day}^{-1}$ at synchronous altitude (using $L=7.37$, as noted above). This result is in line with diffusion coefficients extracted from other data (*cf.* Section IV.7 and Chapter V). The result can be extrapolated to $L\lesssim 4$ by using (4.10) and (4.11) in full, *i.e.*, retaining terms of order ε_1^2, ε_2^2, $\varepsilon_1\varepsilon_2$, and so on. The diffusion coefficient thus calculated for magnetic sudden impulses has the property that $(1/2\tau)\langle(\Delta L_m)^2\rangle$ at $L_m=6.16$ is approximately $(2/3)(6.16)^{10}$ times the value of D_{LL} at $L_m=1$. Since $(dL/dL_m)^2\approx 15/4$ at $L_m=6.16$, it follows that

$$\begin{aligned} D_{LL}&\sim(3/2)(4/15)(L/6.16)^{10}\times 1\,\text{day}^{-1}\\ &\sim 5\times 10^{-9}L^{10}\,\text{day}^{-1} \end{aligned} \tag{4.18}$$

[45] The factor $\{1-[(\gamma+1)/2\gamma](\partial\ln\bar J_\perp/\partial\ln E)_L-(\partial\ln\bar J_\perp/\partial\ln B_e)_E\}$ apparently was *positive* on 22 February 1967 (Fig. 23). The data show a minimum in the flux at $\varphi_3\sim\pi$ and a maximum at $\varphi_3\sim 0$ after a sudden decrease of B_e.

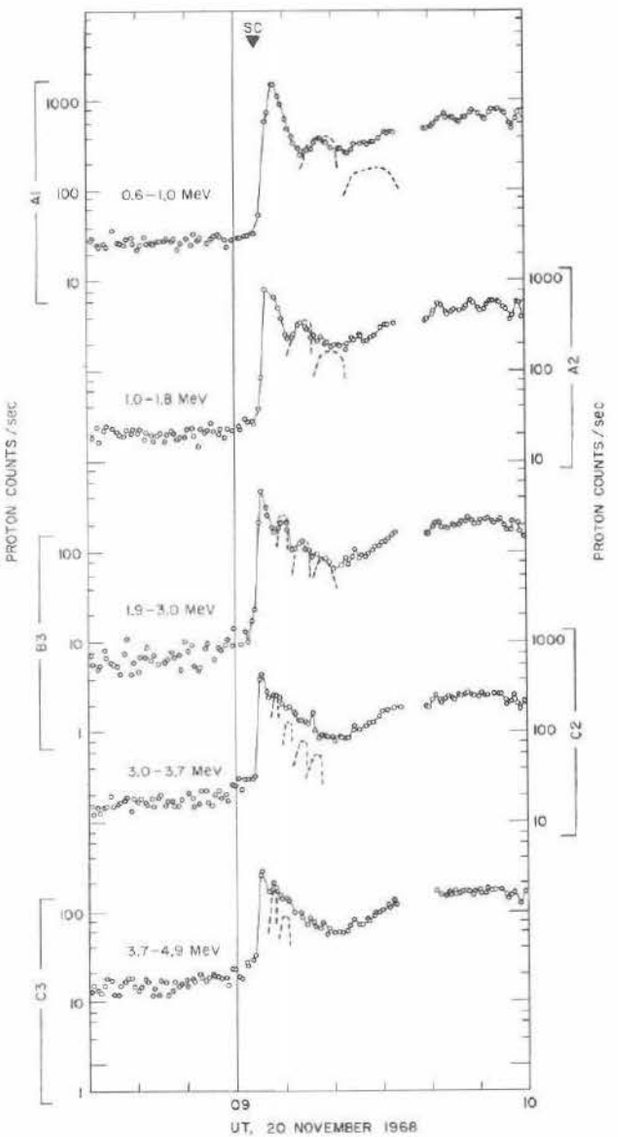

Fig. 67. Evidence of proton drift echoes initiated by sudden commencement at 0904 UT and observed at ATS 1 near local midnight. Dashed curves represent predicted flux modulation based on shape of initial pulse, energy spectrum, and detector response function for each unidirectional channel, assuming a Mead-Williams magnetosphere with $b=9a$ and $B_t=40\gamma$ [110].

at $L\lesssim 4$. It is important, however, to recognize that the parameters inserted in (4.17) to obtain this result are subject to serious uncertainties, and that confidence in the numerical magnitude of this D_{LL} must be tempered accordingly.

Drift echoes have also been detected (following a sudden commencement) in the *proton* flux at ATS 1. As discussed in Section IV.3, proton enhancements and their subsequent decay are frequently observed at synchronous altitude following a sudden change in the earth's magnetic field. The proton data plotted in Fig. 67 show that one or two additional enhancements of the flux follow the initial (large) enhancement that coincides with the sudden commencement [110]. The dashed curves on the figure are the predicted proton intensities, according to a model that the initial flux enhancement is localized in a 30° sector of longitude. The proton spectrum in the model is taken to be the proton spectrum at the peak of the enhancement. As the protons subsequently drift around the earth, they disperse in drift phase. Since the satellite instrument detects protons that vary in energy over a finite "window", the echo of the *sc*-associated enhancement disperses with time. By computer simulation of the detector response, it is found that satisfactory agreement with the observations can be achieved by using a Mead-Williams magnetosphere (see Section I.5) with $b=9a$ and $B_t=40\gamma$.

The protons in Fig. 67 are the solar-flare protons which have relatively free access to the outer regions of the magnetosphere (Section IV.3). Since they undoubtedly experience radial diffusion, it is possible for the magnetosphere to trap some of them. These captured solar-flare protons may ultimately diffuse radially (at constant M and J) into the inner magnetosphere where they would contribute to the high-energy proton population.